CHEMICAL REVIEWS

REVIEW

pubs.acs.org/CR

Localized Surface Plasmon Resonance Sensors

Kathryn M. Mayer[†,§] and Jason H. Hafner[*,†,‡,§]

[†]Department of Physics and Astronomy, [‡]Department of Chemistry, and [§]Laboratory for Nanophotonics, Rice University, Houston, Texas 77005, United States

CONTENTS

1. INTRODUCTION

Localized surface plasmon resonance (LSPR) is a long-studied nanoscale phenomenon of considerable recent interest.[1,2] These resonances, associated with noble metal nanostructures, create sharp spectral absorption and scattering peaks as well as strong electromagnetic near-field enhancements. The past decade has witnessed significant improvements in the fabrication of noble metal nanostructures, which has led to advances in several areas of the science and technology of LSPR. Among these is the detection of molecular interactions near the nanoparticle surface through shifts in the LSPR spectral peak. Here, we offer a general overview of this sensing strategy. As this topic is widespread and growing, we cannot hope for our Review to be comprehensive. We will endeavor, however, to describe the major research efforts in the field and to review a wide and varied cross-section of the relevant literature. We will also present a thorough summary of the physical basis of LSPR sensing and attempt to clarify some ongoing inconsistencies in nomenclature. We focus primarily on LSPR sensors based on metal nanoparticles, rather than extended, fabricated structures. Also, we focus on sensors for which LSPR is the primary mode of signal transduction, rather than hybrid strategies, for example, LSPR combined with fluorescence. Finally, our discussion of biological LSPR sensors is mostly concerned with label-free detection, rather than applications in which the metal nanoparticles act as labels themselves, or serve to enhance the efficiency of a label.

Section 2 of this Review concerns the analytical theory of LSPR: the physical origin of the LSPR itself and its dependence on the material properties of noble metals and the surrounding refractive index. We discuss both spherical and spheroidal particles and describe the dependence of the LSPR on particle aspect ratio. In section 3, we describe the basics of nanoparticle-based LSPR sensing, including a description of single-particle and ensemble measurements, a comparison of scattering, absorption, and extinction, a discussion of how

Special Issue: 2011 Plasmonics

Received: September 18, 2010
Published: June 08, 2011

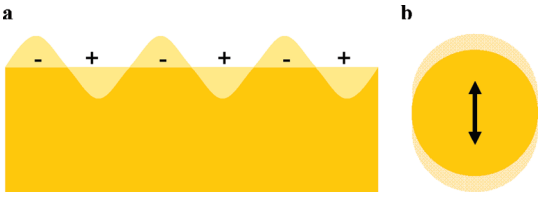

Figure 1. Illustrations of (a) surface plasmons and (b) a localized surface plasmon.

molecular sensitivity might differ from bulk refractive index sensitivity, and a comparison of LSPR sensing with other label-free sensing methods. Section 4 describes in detail some of the many factors that can affect LSPR sensitivity, including nanoparticle shape, size, aspect ratio, and material composition, and includes a detailed comparison among many particle types.

Section 5 is an extensive review of the literature on biological and biomedical LSPR assays. We divide the reports into categories according to the biomolecular interaction employed: biotin/streptavidin binding, antibody/antigen interactions, sugar/lectin interactions, DNA hybridization, and other analyte/receptor interactions. Section 6 reviews chemical (nonbiological) sensing applications of LSPR, including pH sensors, organic vapor sensors, and other chemical sensors. In section 7, we discuss some of the recent technological advancements in LSPR sensing, including incorporating microfluidics, multiplexing, and integrating fiber optic probes. Section 8 reviews the progress toward maximizing the label-free molecular detection sensitivity of LSPR sensors, including few- and single-molecule detection. Finally, in section 9 we discuss the future technological potential of LSPR sensors, including what is still needed to transform current LSPR sensors into viable devices in the laboratory and in the clinic, especially as low-cost medical diagnostic devices.

2. PHYSICS OF LOCALIZED SURFACE PLASMON RESONANCE (LSPR)

2.1. Bulk, Surface, and Localized Surface (Nanoparticle) Plasmons

A plasmon is a collective oscillation of the free electrons in a noble metal. It can be described as a quantum of plasma oscillation (thus the -on suffix); however, this terminology is somewhat misleading as the phenomenon itself can be described accurately by classical physics. One can think of these plasmon oscillations as mechanical oscillations of the electron gas of a metal, the presence of an external electric field causing displacements of the electron gas with respect to the fixed ionic cores. For bulk plasmons, these oscillations occur at the plasma frequency and have energy:

$$E_p = \hbar\sqrt{\frac{ne^2}{m\varepsilon_0}} \tag{1}$$

where ε_0 is the permittivity of free space, n is the electron density, e is the electron charge, and m is the electron mass. (Here, bulk refers to materials with an extent large compared to the wavelength of light in all three dimensions.)

At the surface of a metal, plasmons take the form of surface plasmon polaritons (SPPs), also simply called surface plasmons (Figure 1). Surface plasmons are optically excited, and light can be coupled into standing or propagating surface plasmon modes through a grating or a defect in the metal surface. Because it is the oscillating electric field of the incoming plane wave that excites surface plasmons, light with a high angle of incidence (that is, with wave vector k nearly parallel to the surface) couples most efficiently.

When a surface plasmon is confined to a particle of a size comparable to the wavelength of light, that is, a nanoparticle, the particle's free electrons participate in the collective oscillation, and it is termed a localized surface plasmon (LSP). The LSP has two important effects. First, electric fields near the particle's surface are greatly enhanced, this enhancement being greatest at the surface and rapidly falling off with distance. Second, the particle's optical extinction has a maximum at the plasmon resonant frequency, which occurs at visible wavelengths for noble metal nanoparticles. This extinction peak depends on the refractive index of the surrounding medium and is the basis for the sensing applications, which are the subject of this Review. To understand in depth how this localized surface plasmon resonance (LSPR) arises, we must turn to scattering theory.

2.2. Mie Theory

In the early 20th century, Gustav Mie developed an analytical solution to Maxwell's equations that describes the scattering and absorption of light by spherical particles.[2] (For very small particles ($d \ll \lambda$), Mie scattering agrees with the more familiar Rayleigh scattering.) Finding the scattered fields produced by a plane wave incident on a homogeneous conducting sphere results in the following total scattering, extinction, and absorption cross-sections:[3]

$$\sigma_{sca} = \frac{2\pi}{|k|^2}\sum_{L=1}^{\infty}(2L+1)(|a_L|^2 + |b_L|^2) \tag{2}$$

$$\sigma_{ext} = \frac{2\pi}{|k|^2}\sum_{L=1}^{\infty}(2L+1)[Re(a_L + b_L)] \tag{3}$$

$$\sigma_{abs} = \sigma_{ext} - \sigma_{sca} \tag{4}$$

where k is the incoming wavevector and L are integers representing the dipole, quadrupole, and higher multipoles of the scattering. In the above expressions, a_L and b_L are the following parameters, composed of the Riccati–Bessel functions ψ_L and χ_L:

$$a_L = \frac{m\psi_L(mx)\psi_L'(x) - \psi_L'(mx)\psi_L(x)}{m\psi_L(mx)\chi_L'(x) - \psi_L'(mx)\chi_L(x)} \tag{5}$$

$$b_L = \frac{\psi_L(mx)\psi_L'(x) - m\psi_L'(mx)\psi_L(x)}{\psi_L(mx)\chi_L'(x) - m\psi_L'(mx)\chi_L(x)} \tag{6}$$

Here, $m = \tilde{n}/n_m$, where $\tilde{n} = n_R + in_I$ is the complex refractive index of the metal, and n_m is the real refractive index of the surrounding medium. Also, $x = k_m r$, where r is the radius of the particle. (Note that $k_m = 2\pi/\lambda_m$ is defined as the wavenumber in the medium rather than the vacuum wavenumber.)

To gain insight into LSPR phenomena, simpler expressions than eqs 2–6 are required. If the nanoparticle is assumed to be very small as compared to the wavelength, $x \ll 1$. In this case, the

dx.doi.org/10.1021/cr100313v |Chem. Rev. 2011, 111, 3828–3857

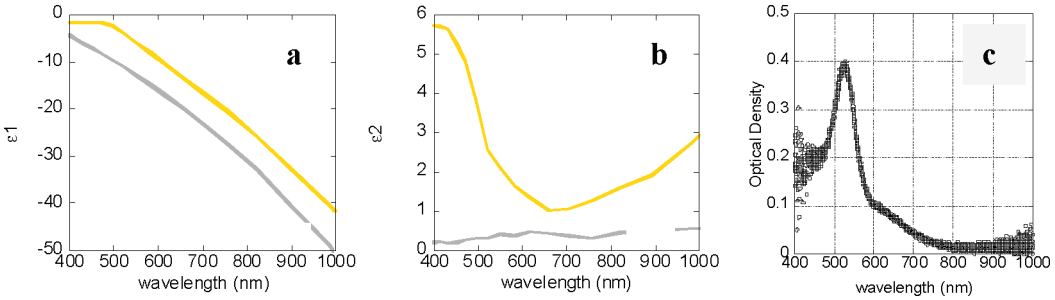

Figure 2. (a) Real and (b) imaginary parts of the complex dielectric functions of silver (lower curves) and gold (upper curves). (c) Absorption spectrum of gold colloid solution.

Riccati−Bessel functions can be approximated by power series. Following Bohren and Huffman,[3] and keeping only terms to order x^3, eqs 5 and 6 simplify to:

$$a_1 \approx -\frac{i2x^3}{3}\frac{m^2-1}{m^2+2} \tag{7}$$

$$b_1 \approx 0 \tag{8}$$

and the higher order a_L and b_L are zero (again, only when keeping terms up to x^3). To find the real part of a_1 as required in eq 3, substitute $m = (n_R + in_I)/n_m$ into eq 7:

$$a_1 = -i\frac{2x^3}{3}\frac{{n_R}^2 - {n_I}^2 + i2n_Rn_I - {n_m}^2}{{n_R}^2 - {n_I}^2 + i2n_Rn_I + 2{n_m}^2} \tag{9}$$

Next, switch to the complex metal dielectric function $\tilde{\varepsilon} = \varepsilon_1 + i\varepsilon_2$ with the following relations:

$$\varepsilon_1 = {n_R}^2 - {n_I}^2 \tag{10}$$

$$\varepsilon_2 = 2n_Rn_I \tag{11}$$

and switch to the medium's dielectric function: $\varepsilon_m = {n_m}^2$. These substitutions lead to:

$$a_1 = \frac{2x^3}{3}\frac{-i{\varepsilon_1}^2 - i\varepsilon_1\varepsilon_m + 3\varepsilon_2\varepsilon_m - i{\varepsilon_2}^2 + i2{\varepsilon_m}^2}{(\varepsilon_1 + 2\varepsilon_m)^2 + (\varepsilon_2)^2} \tag{12}$$

Substitution of eq 12 into eq 3 and taking the dipole term only yields the widely quoted expression for nanoparticle plasmon resonances:

$$\sigma_{ext} = \frac{18\pi\varepsilon_m^{3/2}V}{\lambda}\frac{\varepsilon_2(\lambda)}{[\varepsilon_1(\lambda) + 2\varepsilon_m]^2 + \varepsilon_2(\lambda)^2} \tag{13}$$

where V is the particle volume. A similar process yields the following scattering cross-section:

$$\sigma_{sca} = \frac{32\pi^4{\varepsilon_m}^2V^2}{\lambda^4}\frac{(\varepsilon_1 - \varepsilon_m)^2 + (\varepsilon_2)^2}{(\varepsilon_1 + 2\varepsilon_m)^2 + (\varepsilon_2)^2} \tag{14}$$

While these small particle approximations only strictly apply to very small particles (<10 nm diameter), their predictions of dielectric sensitivity are still accurate for larger particles.[4]

In Figure 2, the complex dielectric functions of bulk silver and gold are plotted, as experimentally determined by Johnson and Christy.[5] The extinction cross-section will be maximized when the denominator in eq 13 is minimized, a condition that will be met when $\varepsilon_1 = -2\varepsilon_m$. This explains the dependence of the LSPR extinction peak on the surrounding dielectric environment. For example, for gold particles in water ($\varepsilon_m \approx 1.7$), the expected wavelength where $\varepsilon_1 = -2\varepsilon_m$ is about 520 nm, according to the real dielectric function for gold. Also, indeed, the experimentally observed absorption spectrum of gold colloid has a strong peak at that wavelength. As this example illustrates, the sensitivity to ε_m originates from the slope of the real part of the dielectric function in the observed wavelength range. Also note that for a given external dielectric constant, the LSPR wavelength for silver will be bluer (shorter) than that for gold. (The dependence of nanoparticles' LSPR properties on their material composition will be discussed in greater detail in section 4.) The imaginary part of the dielectric function also plays a role in the plasmon resonance, relating to the damping, that is, resonance peak broadening, which is observed. Silver suffers lower losses than gold, as implied by Figure 2b; however, gold is often chosen for experiments as it is easier to work with chemically and less prone to oxidation.

Figure 3. Microscope slide with gold colloid. Inscription: "Faraday's gold given to me himself after his lecture at the RI" (Whipple Museum of the History of Science).

Michael Faraday first systematically described the unusual optical properties of gold colloid solution in the midnineteenth century,[1,6,7] calling the solution "a beautiful ruby fluid", and noting that "a mere variation in the size of particles gave rise to a variety of resultant colours." Some of his original gold colloid samples can be seen in Figure 3. Faraday's ideas inspired Mie's later theoretical work that is described above.

2.3. Refractive Index Dependence

To find the functional form of the LSPR peak wavelength's dependence on the dielectric function of the medium,[8] one can

use the analytical, frequency-dependent form for ε_1 from the Drude model of the electronic structure of metals:

$$\varepsilon_1 = 1 - \frac{{\omega_p}^2}{\omega^2 + \gamma^2} \quad (15)$$

where ω_p is the plasma frequency and γ is the damping parameter of the bulk metal. (The Drude model is a purely classical model of electronic transport in conductors. It describes the collisions between freely moving electrons and a lattice of heavy, stationary ionic cores; it provides a very good approximation of the conductivity of noble metals.) For visible and near-infrared frequencies, $\gamma \ll \omega_p$ so the above can be simplified to:

$$\varepsilon_1 = 1 - \frac{{\omega_p}^2}{\omega^2} \quad (16)$$

Using this expression for ε_1 and setting $\varepsilon_1 = -2\varepsilon_m$ (the resonance condition), one obtains the following:

$$\omega_{max} = \frac{\omega_p}{\sqrt{2\varepsilon_m + 1}} \quad (17)$$

where ω_{max} is the LSPR peak frequency. Converting from frequency to wavelength via $\lambda = 2\pi c/\omega$, and then from dielectric constant to index of refraction via $\varepsilon_m = n^2$, the above expression becomes:

$$\lambda_{max} = \lambda_p \sqrt{2{n_m}^2 + 1} \quad (18)$$

where λ_{max} is the LSPR peak wavelength and λ_p is the wavelength corresponding to the plasma frequency of the bulk metal. Thus, we see that the dependence of LSPR peak wavelength on the refractive index ought to be approximately linear at optical frequencies; this is borne out in experiments. Equation 18 is plotted for λ_p = 300 nm over a reasonable range of n in Figure 4. Note that neither the LSPR peak frequency/energy nor wavelength is strictly linear with refractive index, but both are approximately linear over small ranges of n.

2.4. Gans Theory

Mie theory as formulated above is strictly applicable only to spherical particles. In 1912, Richard Gans generalized Mie's result to spheroidal particles of any aspect ratio in the small particle approximation.[9] He found that the absorption cross-section for a prolate spheroid, analogous to that in eq 13 above for a sphere, is:

$$\sigma_{abs} = \frac{\omega}{3c}\varepsilon_m^{3/2} V \sum_j \frac{(1/P_j^2)\varepsilon_2}{\{\varepsilon_1 + [(1-P_j)/P_j]\varepsilon_m\}^2 + \varepsilon_2^2} \quad (19)$$

Here, the sum over j considers the three dimensions of the particle. P_j includes P_A, P_B, and P_C, termed depolarization factors, for each axis of the particle, where A > B = C for a prolate spheroid. The depolarization factors anisotropically alter the values of ε_1 and ε_2 and the resulting LSPR peak frequencies. Explicitly, they are:

$$P_A = \frac{1-e^2}{e^2}\left[\frac{1}{2e}\ln\left(\frac{1+e}{1-e}\right) - 1\right] \quad (20)$$

$$P_B = P_C = \frac{1 - P_A}{2} \quad (21)$$

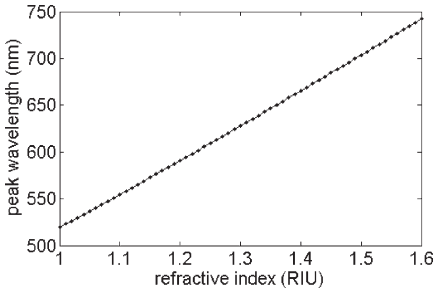

Figure 4. The nearly linear dependence of LSPR peak wavelength on refractive index based on the Drude model.

where e is the following factor, which includes the particle aspect ratio R:[10−12]

$$e = \left[1 - \left(\frac{B}{A}\right)^2\right]^{1/2} = \left(1 - \frac{1}{R^2}\right)^{1/2} \quad (22)$$

The extinction spectrum resulting from eq 19 has two peaks, one corresponding to the transverse plasmon mode from the x and y contributions to the sum, and the other corresponding to the longitudinal plasmon mode from the z contribution. Equation 19 also provides an intuitive understanding of the effect of aspect ratio on the LSPR peak wavelength. The factor weighting ε_m, which is 2 for spherical particles, is $[(1 - P_j)/P_j]$, a quantity that increases with aspect ratio and can be much greater than 2. This leads to a red-shift of the plasmon peak with increasing aspect ratio, as well as increased sensitivity to the dielectric constant of the surrounding medium (see Figure 5).

For nanoparticles beyond these spheres and spheroids, particle shape plays a significant role in determining the LSPR spectrum,[13,14] but one that cannot be found analytically as above, and must be studied numerically. Numerical methods for plasmonic nanoparticles include finite difference time domain (FDTD), discrete dipole approximation (DDA), and finite element method (FEM). An excellent introduction to these three methods can be found in the review by Zhao, Schatz, et al.[15] The effect of particle shape on the LSPR spectrum and refractive index sensitivity will be discussed in detail in section 4.

3. SENSING WITH LSPR

3.1. Refractive Index Sensing

The simplest sensing application of LSPR-active particles is to detect changes in the bulk refractive index of their environment through shifts in the LSPR peak wavelength. LSPR peaks are typically detected by spectral extinction measurements on a dense film or spectral scattering measurements on single nanoparticles. Figure 6 displays spectra of three nanoparticle shapes, highlighting the differences in these two types of measurements. All of the spectra shown in Figure 6 are for particles immobilized on glass substrates and exposed to air. For small gold nanorods, the ensemble extinction has two strong peaks corresponding to the transverse and longitudinal modes of the particles, but the single-particle scattering is too weak to be seen, as the extinction is dominated by absorption. However, for larger nanorods, scattering makes up a larger portion of the extinction and can be measured.[16] For gold nanostars, the extinction is largely due to scattering, but there is an important distinction between ensemble and single-particle measurements. Individual nanostars'

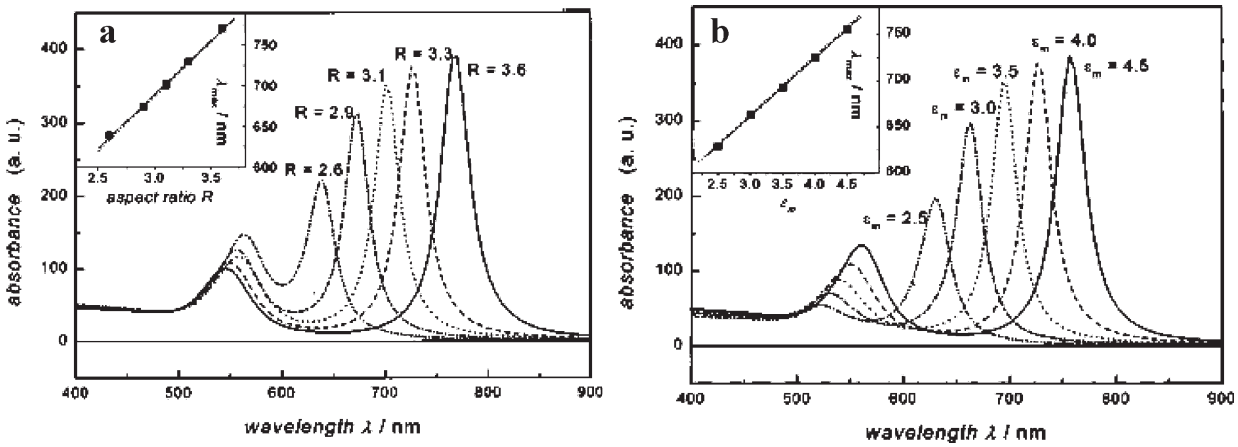

Figure 5. Gans theory calculation for gold nanorods. (a) Dependence of absorbance spectrum on aspect ratio for a constant dielectric constant of the medium (inset: peak wavelength increases linearly with aspect ratio). (b) Dependence of absorbance spectrum on dielectric constant of the medium for a constant aspect ratio (inset: peak wavelength increases linearly with dielectric constant). Reprinted with permission from ref 12. Copyright 1999 American Chemical Society.

spectra vary greatly depending on their exact structure, and so in the single-particle spectrum, separate peaks corresponding to the arms of the nanostar can be seen, whereas the ensemble extinction is simply a broad peak made up of many overlapping spectra.[17,18] For gold bipyramids, the ensemble extinction has two peaks, one due to the bipyramids and one due to other shapes including spheres in the sample. When single-particle scattering spectra are taken, a single peak due to the bipyramid is seen. For small particles that do not scatter strongly, ensemble extinction methods are best, whereas for larger particles that scatter brightly, single-particle dark field scattering measurements are possible.

As discussed in section 2.3, the LSPR peak wavelength shift is approximately linear with changes in refractive index of the surrounding medium. Therefore, the refractive index sensitivity S of a particular nanoparticle type is usually reported in nanometers of peak shift per refractive index unit (nm/RIU).

$$S = \frac{d\lambda_p}{dn} \tag{23}$$

An example of this type of sensing is shown in Figure 7 for a gold nanorod film in a series of solvents of different refractive indices: air (n = 1.000), water (n = 1.333), ethanol (n = 1.361), and formamide (n = 1.428). Note that, although the plasmon resonance wavelength is not strictly linear with index of refraction, it is linear to a good approximation over small ranges of n. (See Figure 5 in section 2.3 and the accompanying discussion.)

Because LSPR sensing is based on spectral peak shifts, the precision that can be achieved with respect to changes in the refractive index depends on the sensitivity, S, and the peak line width. Larger nanoparticles tend to have high sensitivities, but their peaks are broadened by multipolar excitations and radiative damping. A figure of merit (FOM) obtained by dividing the sensitivity by the resonance line width[21] is widely used to characterize a nanoparticle's sensing capabilities. (See Figure 8.)

$$\text{FOM} = \frac{S}{\Delta\lambda} \tag{24}$$

Although the sensitivity and figure of merit were both initially defined in terms of wavelength, many in the field prefer to define the shift in terms of resonance energy when analyzing LSPR spectra (usually in electron volts, eV),[22,23] and we therefore use both unit systems in our table comparing the sensitivities of various nanoparticles; see section 4. While there is some debate as to whether nm/RIU or eV/RIU is most appropriate, note that the LSPR shift is not strictly linear with n in either unit. The more important consideration is simply that the chosen units are used consistently across any comparison. One can see this from eq 18 for wavelength. Converting to energy units (eV) and rearranging eq 18 shows that E is also not linear with n:

$$E = \frac{hc}{\lambda_p\sqrt{2n_m^2 + 1}} \tag{25}$$

However, given the narrow spectral range that is probed in practice, the LSPR shift is approximately linear with n in both unit systems at visible frequencies. (See Figure 9; recall Figure 4 from section 2.3.)

Recently, Becker et al. have suggested an alternative figure of merit, termed FOM*, as a more general metric for comparison between different nanostructures' sensing ability.[24] Because it is difficult to define a consistent LSPR line width $\Delta\lambda$ for some of the more complex plasmonic nanostructures (metamaterials, etc.), which lack a simple, single line shape, FOM* is defined in terms of the relative intensity change dI/I that occurs at a given wavelength λ_0 upon a small change dn to the local refractive index and does not include the line width. This way, sensors based on changes in intensity and those based on peak shifts can be directly compared. For the latter type, FOM* can be written in terms of refractive index sensitivity S.

$$\text{FOM}^* = \left(\frac{\frac{dI}{dn}}{I}\right)_{max} = \left(\frac{\frac{dI}{d\lambda}\cdot\frac{d\lambda}{dn}}{I}\right)_{max} = \left(\frac{S\frac{dI}{d\lambda}}{I}\right)_{max} \tag{26}$$

Note that FOM* is defined for whichever wavelength gives the maximum intensity change with refractive index. FOM* can also be expressed in terms of the sensitivity in (nm/RIU); see the final expression in eq 26. Figure 10 illustrates the subtle difference between FOM and FOM* for gold nanorods of varying aspect ratios. The maximum FOM occurs for nanorods of aspect ratio

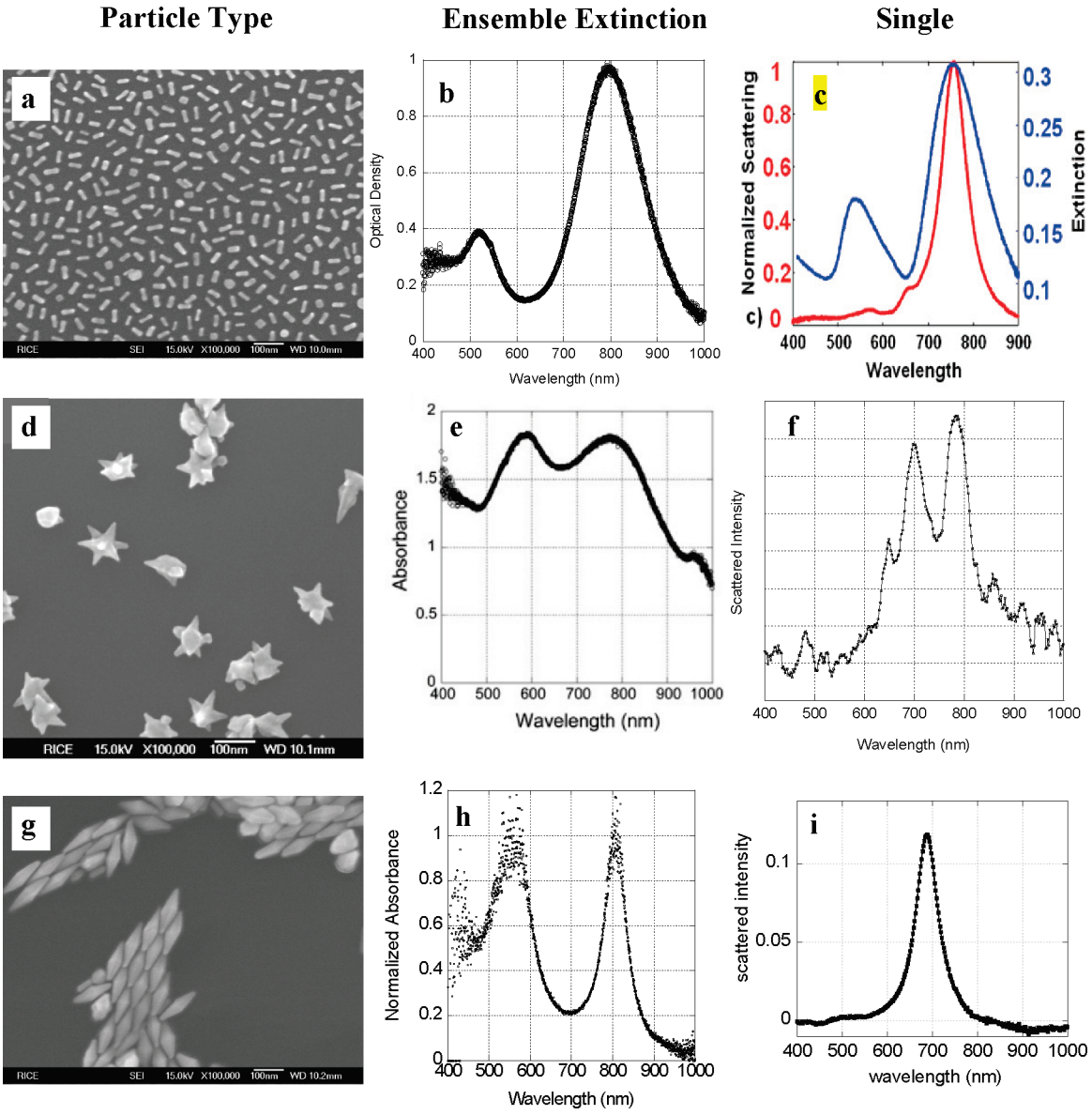

Figure 6. Comparison of the ensemble extinction and single-particle scattering spectra for three particle types. (a) Gold nanorods. (b) Nanorod ensemble extinction. The two peaks are attributed to the transverse and longitudinal plasmon modes of the particle. (c) The nanorods shown in (a) and (b) scatter too weakly to obtain single-particle scattering spectra. However, for larger nanorods scattering may be measured. (d) Gold nanostars. (e) Nanostar ensemble extinction. Individual particle spectra are smeared out into a single broad peak in the near IR. (f) Nanostar single-particle scattering spectrum. Multiple peaks in the near IR correspond to resonances of the arms of the star. (g) Gold bipyramids. (h) Bipyramid ensemble extinction. Two peaks are visible, attributable to bipyramids and spheres. (i) Bipyramid single-particle scattering spectrum. A single bright, narrow peak is seen. It occurs at a wavelength different from that of (h) because the particle came from a different batch and therefore different aspect ratio of gold bipyramids. Reprinted with permission from refs 16,17,19,20. Copyright 2006, 2008, 2009 American Chemical Society.

4.3; these nanorods would be best for applications based on LSPR spectral peak fitting. The maximum FOM* occurs for slightly lower aspect ratio nanorods (AR = 4.2); these would be best for applications based on measuring intensity changes at a fixed wavelength.

3.2. Molecular Sensing

While LSPR sensors can detect changes in bulk refractive index for calibration, they are unique for their localized sensing capabilities. As described in section 4.2, field enhancements due to LSPR decay rapidly with distance from the nanoparticle surface; therefore, spectral LSPR shifts only probe a nanoscale region around the particle. This highly localized sensing volume allows one to observe molecular interactions near the nanoparticle surface because they result in changes in the local refractive index. See Figure 11 for an illustration of the contrast between bulk and molecular sensing by LSPR.

A process that demonstrates molecular sensing by LSPR and clearly illustrates the localized sensing volume of nanoparticles is self-assembled monolayer (SAM) formation on the nanoparticle surface. SAMs of alkane thiols are a facile and well-known surface modification of gold and silver (plasmonic) nanostructures. Malinsky, Haes, et al. have measured the LSPR shift upon monolayer formation on silver nanotriangles fabricated via nanosphere

dx.doi.org/10.1021/cr100313v |*Chem. Rev.* 2011, 111, 3828–3857

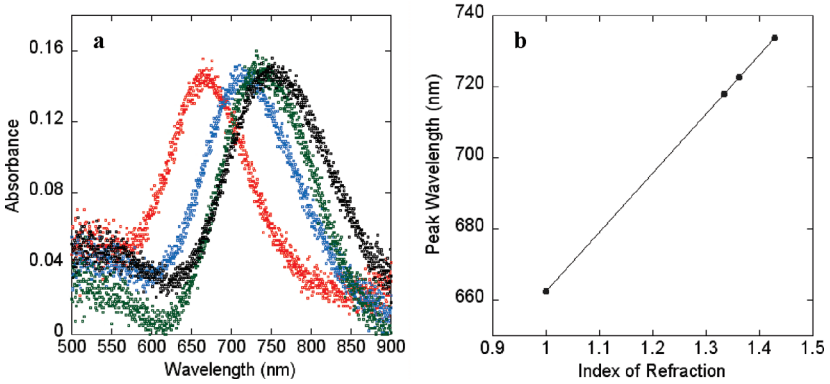

Figure 7. (a) Optical absorbance of gold nanorod film in air (red), water (blue), ethanol (green), and formamide (black). (b) Plotting the peak wavelength versus index of refraction yields a sensitivity (slope) of 170 nm/RIU. Reprinted with permission from ref 19. Copyright 2008 American Chemical Society.

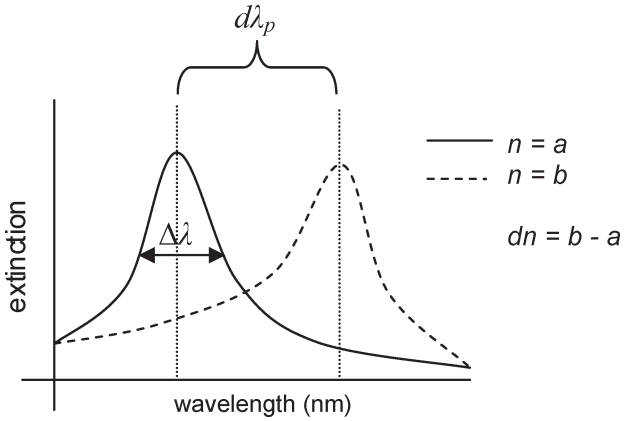

Figure 8. Definition of the LSPR figure of merit (FOM). See eqs 23 and 24.

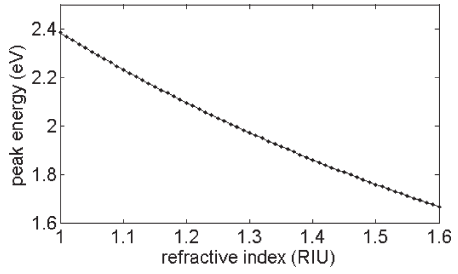

Figure 9. The nearly linear dependence of LSPR energy in electron volts on refractive index based on the Drude model. Compare to Figure 4 in section 2.3.

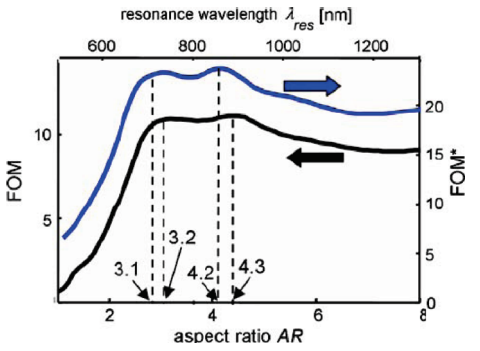

Figure 10. FOM and FOM* for gold nanorods of varying aspect ratio, as calculated in boundary element method simulations. (The double *x*-axis here highlights the fact that LSPR wavelength is linear with nanorod aspect ratio.) Reprinted with permission from ref 24. Copyright 2010 Springer.

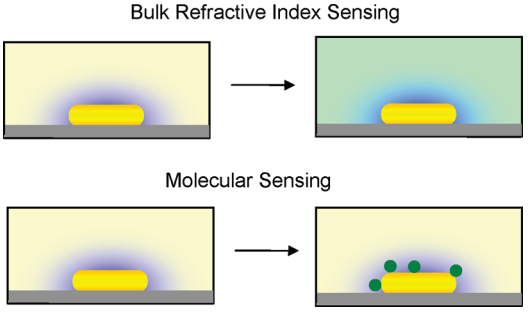

Figure 11. Bulk refractive index sensing versus molecular sensing by LSPR. In the latter case, the change to the particle's dielectric environment is confined to the sensing volume.

lithography.[25−27] SAMs of varying carbon chain lengths were used, and the researchers were able to measure the LSPR shifts as the SAM length increased one CH_2 group at a time. In addition, they described how the LSPR sensitivity falls off with distance from the surface using SAMs of increasing length. (See Figure 12.) In Figure 12a, SAMs of varying alkane chain lengths (from 2 to 17 carbon atoms) showed a linear dependence of LSPR peak wavelength on layer thickness up to 3 nm from the particle surface. In Figure 12b, successive SAM layers were deposited in alternation with copper ions to build up SAM mutilayers that extended from 2 to 34 nm from the particle surface. In this case, note that the LSPR shift per added layer begins to level off for films thicker than approximately 20 nm. This information is very important for the design of biosensors, indicating that the thickness of capture layers should be minimized, and in particular must be kept to less than 20 nm so that the shift due to target binding is observable. It also indicates that one must be very careful to differentiate the bulk refractive index sensitivity of a nanoparticle from its molecular detection sensitivity, because the details of the particle's surface structure and its environment are extremely important to the latter.

Nusz et al. have proposed a metric for comparing different nanoparticles' molecular detection sensitivity, which they term a

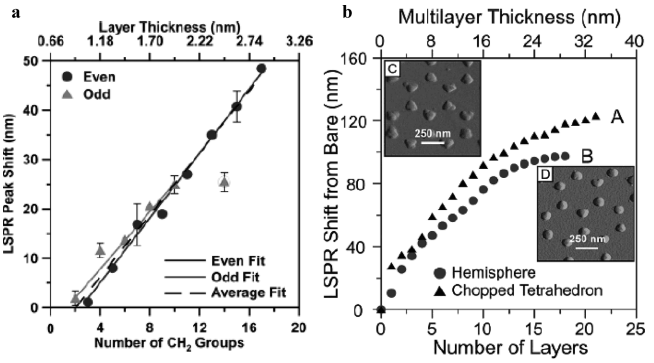

Figure 12. LSPR molecular detection sensitivity dependence on distance from particle surface. (a) Detecting short SAMs of varying length. (b) Detecting longer SAM multilayers. Reprinted with permission from refs 26,27. Copyright 2004 American Chemical Society.

figure of merit, although it is distinct from the figure of merit described in section 3.1.[28] Here, we will refer to it as FOM_{mol} to distinguish the two. Essentially FOM_{mol} is defined as the maximum number of bound molecules on the nanoparticle (or dynamic range, DR) divided by the minimum number of detectable molecules (or molecular detection limit, MDL). The authors estimated the DR simply from the nanoparticle's available surface area. The MDL was calculated as:

$$\mathrm{MDL} = \frac{V_S\sqrt{U_{\mathrm{system}}^2 + U_{\mathrm{fit}}^2}}{V_A \cdot \Delta\mathrm{RI} \cdot e^{-2r/l_d} \cdot 3S_0} \qquad (27)$$

where V_S is the sensing volume, V_A is the analyte volume, ΔRI is the refractive index difference between the analyte and the surrounding medium, U_{system} is the uncertainty in the physical detection of the LSPR peak, U_{fit} is the uncertainty in the fitting of the LSPR peak, S_0 is the bulk refractive index sensitivity, r is the distance from the particle surface to where the analyte binds, and l_d is the decay length of the electric field from the particle surface. See Figure 13 for an illustration of the geometric parameters.

For gold nanorods, all of the parameters in eq 27 can be determined analytically or experimentally, and the authors determine that the ideal nanorod geometry for molecular detection of streptavidin is approximately 60 nm by 30 nm, with a predicted MDL of 18. Interestingly, Becker et al. performed a similar analysis based on their definition of FOM* and concluded that the optimal nanorod geometry for sensing should have an aspect ratio between 3 and 4.[24] Becker et al. also proposed another figure of merit in which the local sensing volume is taken into account. For a film of target biomolecules of average thickness l and a known refractive index, they defined a figure of merit for thin layers to be:

$$\mathrm{FOM}^*_{\mathrm{layer}} = \left(\frac{\mathrm{d}I}{\frac{I}{\mathrm{d}l}}\right)_{\mathrm{max}} \qquad (28)$$

Here, I is the initial intensity at the wavelength that experiences the maximum intensity change with refractive index.

Note that because it relies on a simplistic model for the analyte density on the surface, and does not take into account spatial variations (e.g., increased refractive index sensitivity at sharp tips), the FOM_{mol} metric uses a simple model for the analyte density on the surface and does not account for spatial variations in sensitivity across the particle; however, it does provide a great deal of insight to factors other than the bulk refractive index sensitivity that influence the molecular detection sensitivity of plasmonic nanoparticles.

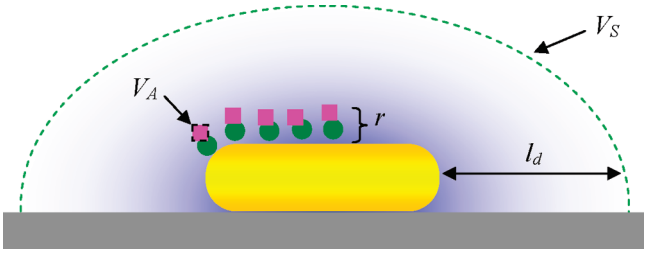

Figure 13. Schematic of the geometric parameters in eq 27 for the example of a gold nanorod.

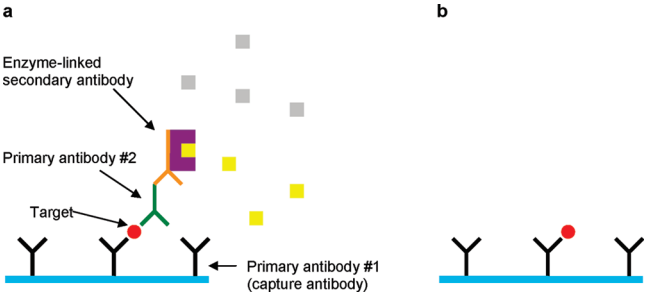

Figure 14. Schematics of (a) a traditional immunoassay (ELISA) and (b) a label-free immunoassay.

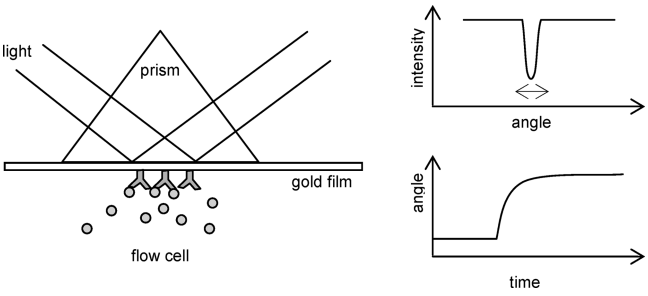

Figure 15. Schematic of a surface plasmon resonance (SPR) sensor.

3.3. Comparison with Other Label-Free Methods

In a label-free sensor, the measured signal is due only to the presence of the target molecule. Because LSPR directly detects the target's refractive index, it fits into this category. This is in contrast to the vast majority of biological sensors, which rely on labels to generate and amplify the target signal. In most immunoassays, for instance, a "sandwich" strategy is employed, in which a labeled antibody is used after target capture.[29] Depending on the technique, the labels can be radioisotopes, fluorophores, or enzymes. For example, enzyme-linked immunosorbant assay (ELISA) relies on an enzyme that activates a dye molecule when bound to the target. (See Figure 14.) Labeling strategies allow biologists to measure signals from miniscule amounts of sample due to their great amplification, for example, thousands of dye molecules activated for each target protein. However, labels can affect interactions, so for detailed studies of biomolecules in their

dx.doi.org/10.1021/cr100313v |Chem. Rev. 2011, 111, 3828–3857

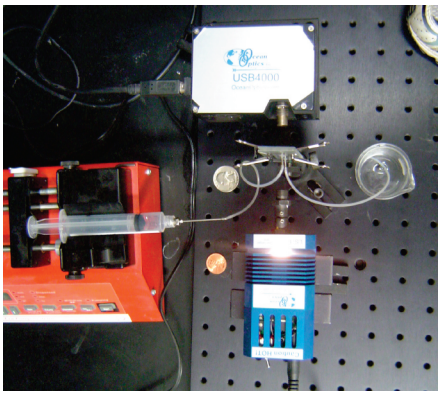

Figure 16. A simple benchtop LSPR system.

natural state (or as close as possible), label-free techniques are preferred. In addition, label-based techniques are necessarily carried out as end point assays; that is, the target is detected through a signal measured before and after analyte exposure. Label-free techniques provide kinetics data, as described below. In terms of immunoassays, label-based methods usually require two or more antibodies to the target molecule, whereas label-free assays require only one.

A similar technique to LSPR sensing is surface plasmon resonance (SPR) sensing. SPR utilizes the sensitivity of surface plasmon polaritons on a gold film to changes in refractive index, usually measured as the change in reflected laser light passed through a prism and reflected off of the back of the film.[30] Due to surface plasmon resonance in the gold film, the reflectance has a minimum at a specific wavelength and angle (See Figure 15). SPR is a powerful surface analytical technique because it can detect submonolayer quantities of analyte at the gold film surface and provide kinetics data through continuous optical measurements. One drawback is that SPR sensors lack a localized sensing volume, in many cases necessitating a thick polymer layer or matrix to cover the gold film surface that must be suffused with the capture antibody to generate a detectable binding signal.

SPR has become widely used in the study of biomolecular interactions, as well as in antibody screening for diagnostic and therapeutic applications.[31,32] However, despite its analytical capabilities, SPR is not widely used in clinical immunoassays or other nonresearch applications, partly due to its lower sensitivity as compared to ELISA and other techniques, but also due to the complexity of the optical instrumentation and the need for precise temperature control. It has been suggested that LSPR sensing with nanoparticle substrates will preserve the virtues of SPR but greatly broaden the scientific and technological applications, because LSPR sensing is based on a simple optical extinction measurement, is not temperature sensitive, and requires only common laboratory equipment.[33] Furthermore, nanoparticles have a highly localized LSPR sensing volume, which eliminates the need to trap the interacting molecules of interest in a polymer matrix to enhance the signal, as is often done in SPR measurements. Despite these successes, and the simple setup for LSPR (see Figure 16), LSPR sensing is still not nearly as prevalent as SPR. For a comparison of SPR and LSPR, see Table 1.

SPR and LSPR have been compared side-by-side experimentally by Yonzon et al. for concanavilin A (ConA) binding to monosaccharides on the surface of silver nanoparticles.[34]

Table 1. Overall Comparison of LSPR and SPR Sensors, Adapted from Reference 33

	LSPR	SPR
bulk dielectric sensitivity (nm/RIU)	10^2	10^6
sensing distance (nm)	10	1000
temperature sensitive?	no	yes
simple instrumentation?	yes	no

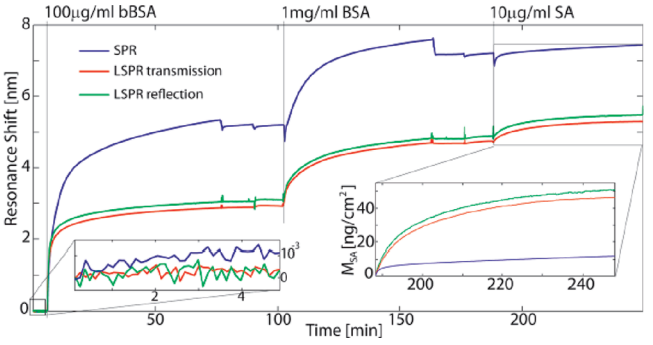

Figure 17. Side-by-side comparison of SPR and LSPR biosensing. Inset: Adsorbed mass of streptavidin in ng/cm^2. Reprinted with permission from ref 35. Copyright 2000 American Chemical Society.

Qualitatively similar binding and unbinding curves were seen for the two techniques, although the unbinding signal in LSPR was smaller. The authors speculate that, due to the smaller sensing volume, only those molecules that were tightly bound were measured. The signal-to-noise ratio was much higher for SPR than LSPR in these experiments. Later, Svedendahl et al. carried out a more detailed experimental comparison of the two methods in which biotin−streptavidin binding was observed under identical experimental conditions in an SPR system with excitation at 700 nm, and in an LSPR system based on a fabricated array of gold nanodiscs with its plasmon resonance at the same wavelength.[35] The LSPR data were measured in terms of both reflectance and absorbance. They found that, although the bulk refractive index sensitivity is higher for SPR, the two techniques exhibited similar performance in the molecular sensing experiment, which they attribute to the long decay length of propagating plasmons as compared to the localized nanoparticle plasmon modes. The resonance wavelength shifts upon streptavidin binding for both techniques are quite similar, but because the gold surface area on the LSPR substrate is about one-fourth of that on the SPR substrate, the authors point out that the detectivity in ng/cm^2 (target mass per unit surface area, a common metric for SPR sensors) is actually better in the LSPR case. (See Figure 17, right inset.) The signal-to-noise ratios of the techniques were also similar in this study (left inset).

Ahl, Yu, et al. have reported a novel nanoporous gold substrate produced by a chemical dealloying method that can support both propagating surface plasmons (SPR modes) and localized surface plasmons (LSPR modes).[36,37] They deposited multiple layers of dendrimers and showed the decay of LSPR molecular detection sensitivity with distance from the surface, similar to the demonstration with SAMs in Figure 12. Simultaneously, they monitored the SPR signal and showed that it does not depend on distance from the surface, at least up to 18 dendrimer layers (a thickness of approximately 17 nm). (See Figure 18.)

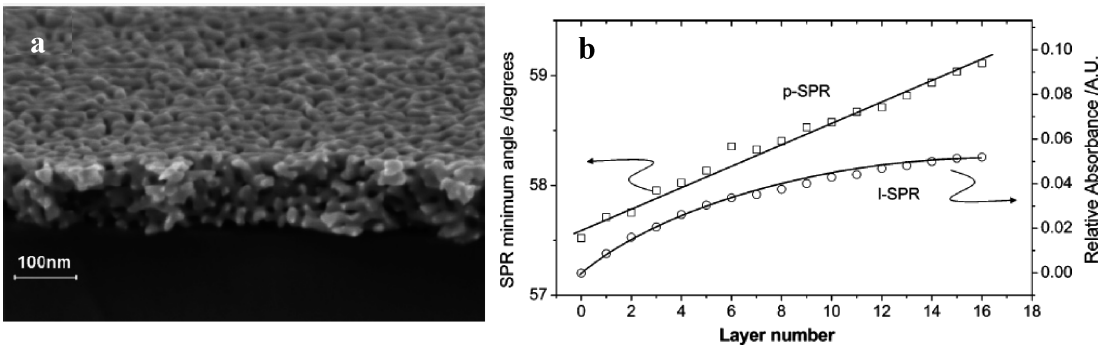

Figure 18. (a) The nanoporous gold film of Ahl, Yu, et al. (b) Dependence of SPR and LSPR signals on distance from the surface, as measured by successive deposition of dendrimer layers. Reprinted with permission from ref 36. Copyright 2006 American Chemical Society.

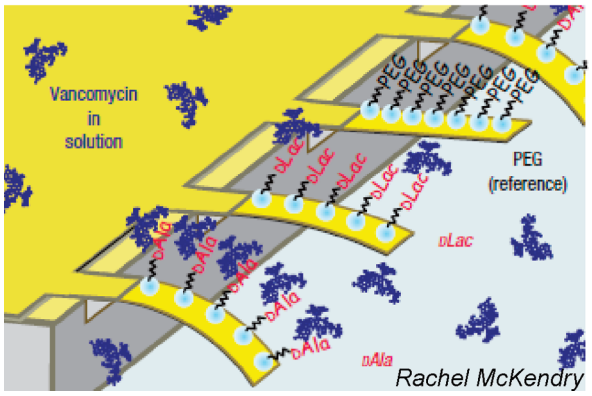

Figure 19. Label-free biosensing based on force sensors. Reprinted with permission from ref 38. Copyright 2008 Nature Publishing Group.

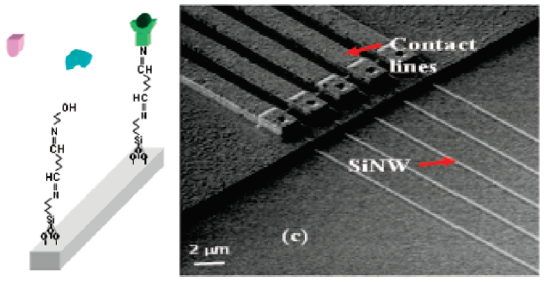

Figure 20. Label-free biosensing based on semiconductor nanowires. Reprinted with permission from ref 39. Copyright 2009 American Chemical Society.

Looking beyond SPR and other optical methods, label-free biosensing can be achieved through force transduction. For example, one can measure the bending of an AFM-like cantilever with a functionalized surface due to the added mass and altered surface tension upon target binding. This technique has recently been used by Ndieyira et al. to investigate the mechanisms of antibiotic drug resistance in bacteria by measuring the affinity of vancomycin (an antibiotic) for an array of target mucopeptides (molecules found on bacterial cell walls) in a multiplexed experiment, in which multiple cantilevers were modified with different ligands. Vancomycin concentrations as low as 10 nM were successfully detected.[38] (See Figure 19.)

Label-free biosensing has also been achieved electronically in semiconductor nanowire systems in which the sensing mechanism consists of measuring the change in conductance through the nanowire upon binding of a charged target, such as a protein molecule. This technique has recently been used by Chua et al. for ultrasensitive label-free detection of the human blood protein cardiac troponin-T (cTnT), an important biomarker of myocardial infarction (heart attack). In that study, silicon nanowires were functionalized with antihuman cTnT to introduce specificity, and cTnT was subsequently measured at concentrations as low as 1 fg/mL (3 aM).[39] (See Figure 20.)

4. EFFECTS OF PARTICLE SIZE, SHAPE, AND MATERIAL

4.1. Nanoparticle Size and Aspect Ratio

For metal nanoparticles of a given shape and material composition, the LSPR properties depend strongly on the particle size. According to Mie theory, for spherical particles of radius R much smaller than the wavelength of light ($2\pi R \ll \lambda$), the magnitude of the scattering cross-section is proportional to R^6, while absorption is proportional to R^3. Because of the prefactors, for the smallest particles, LSPR extinction is dominated by absorption, and as particle size increases, scattering takes over. For gold nanospheres, this transition occurs at around 80 nm in particle diameter.[40] This is in addition to the well-known dependence of plasmon resonance wavelength on particle size. For gold nanospheres, the LSPR wavelength can be tuned over 60 nm by varying particle size between 10 and 100 nm.[41] This effect was noted as early as 1909 by Gustav Mie's contemporary Richard Zsigmondy, who carried out early dark field microscopy studies of gold colloid (see Figure 21). The plasmon resonance line width also varies with particle size, due to a combination of interband transitions, which contribute to increased line width for small particles, and higher-order (nondipole) plasmon modes, which contribute to increased line width for larger particles.[41]

As described in section 2.4, the refractive index sensitivity for spheroidal particles is determined not only by the material composition and the particle size, but also the aspect ratio.[11,12] Elongated nanoparticles like gold and silver nanorods and bipyramids are well-described by spheroidal models, and the predicted aspect ratio dependence is borne out in experiments. For example, for gold nanorods with radius of 10 nm, Lee et al. showed that the sensitivity increases from 157 to 497 nm/RIU for aspect ratio increasing from 1.0 (spheres) to 3.4. For nanorods of the same aspect ratio but different sizes, the larger nanorods have higher refractive index sensitivity.[42] As another example, for gold bipyramids, Chen et al. showed that the sensitivity increases from 150 to 540 nm/RIU for aspect ratio

dx.doi.org/10.1021/cr100313v |Chem. Rev. 2011, 111, 3828–3857

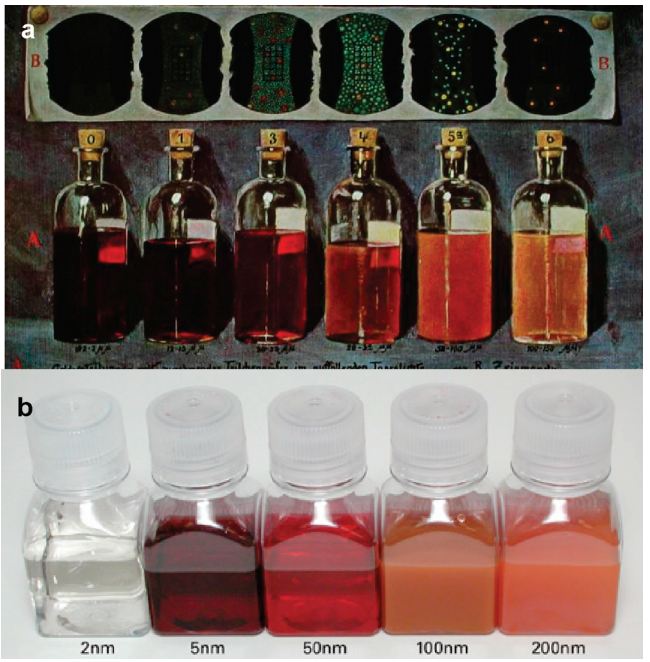

Figure 21. Size dependence of gold colloid optical properties. (a) 1909 illustration of dark field scattering of gold colloid of various sizes. (b) Modern photograph of similar colloid solutions (Ted Pella Co.).

increasing from 1.5 to 4.7, although in this study the particle radius also varied.[43] Slaughter et al. have also demonstrated the separate but related effects of particle radius and aspect ratio.[44]

4.2. Nanoparticle Shape

The LSPR sensitivity of nonspheroidal particles cannot be described analytically, but it has been shown experimentally and in electrodynamic simulations[45] that particle shape plays a large role in determining the sensitivity. In particular, particles with sharp tips produce much higher refractive index sensitivities than would be predicted from their aspect ratios alone. Over the past decade, a myriad of new nanoparticle shapes with ever increasing refractive index sensitivities have been developed.

The effect of particle shape on LSPR properties was dramatically demonstrated in the work of Mock et al., in which the spectra of silver nanoparticles of different shapes (spheres, triangles, and cubes) but similar volume were correlated with their structure.[14] In addition, the particles' refractive index sensitivity was characterized at the single-particle level, and it was determined that silver nanotriangles had a much higher sensitivity (350 nm/RIU) than spheres (160 nm/RIU).[53] As another example, Sun et al. demonstrated the difference in refractive index sensitivity between gold nanospheres and nanoshells of the same diameter. They showed that the nanoshells had a much higher sensitivity (409 nm/RIU) as compared to the spheres (60 nm/RIU).[47] Particles with sharp tips (nanotriangles, bipyramids) exhibit especially high refractive index sensitivities.[56,58]

It is important to distinguish whether these varying refractive index sensitivities are simply due to the varying plasmon resonance wavelengths of the particles (via the metal's optical properties at that wavelength), or if there are intrinsic effects of particle shape at play. In general, for a given material composition, the more red-shifted (lower in energy) a plasmon resonance is, the higher is its refractive index sensitivity.[45] As seen in theoretical work from Miller and Lazarides, nanoparticle refractive index sensitivity

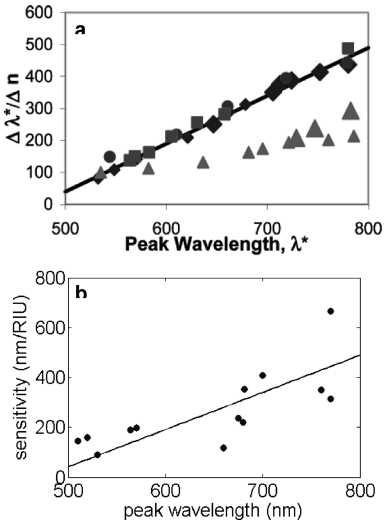

Figure 22. (a) Theoretical predictions of refractive index sensitivity for hollow nanoshells (◆), dielectric-core nanoshells (▲), discs (■), and cylinders (●) of varying plasmon resonant wavelength. Reprinted with permission from ref 45. Copyright 2005 American Chemical Society. (b) Sensitivity versus peak wavelength for the particles in Table 2, with solid line from (a) overlaid.

varies linearly with plasmon resonant wavelength.[45] As seen in Figure 22, hollow nanoshells, nanodiscs, and nanocylinders all fall on the same line in a plot of sensitivity versus peak wavelength. This implies that intrinsic shape effects are much smaller than the plasmon resonance wavelength effect. However, for nanoshells with a dielectric core, the slope decreases relative to that of solid metal nanoparticles, due to the plasmon damping effect of the dielectric material. The trend predicted by Miller and Lazarides for the solid metal nanoparticles matches fairly well with the data for the various particle types described in the table above, although it does not hold perfectly, especially for the more exotic shapes such as nanostars. (See Figure 22.) Also note that particle size does not appear in these graphs. Ultimately, factors of particle shape, size, and plasmon resonance wavelength are all interrelated and all contribute to the refractive index sensitivity, and these factors are further conflated with effects of material composition of the particles, with substrate effects, and, in the case of core−shell particles, with additional dielectric effects.

There has been a great deal of interest in nanoparticle shapes with sharp features or tips, which have been developed through both bottom-up (chemical synthesis) and top-down (lithography) methods. Some of these include silver[21] and gold[43] nanocubes, gold nanostars,[17] silver nanotriangles,[59] gold bipyramids,[60] and gold nanocrescents.[54] One effect of the sharp tips is to produce a red shift in the plasmon resonance,[61−63] increasing the refractive index sensitivity as discussed above. However, note that sharp features will present an additional advantage for molecular detection at the microscopic level in that a sharp tip creates a localized sensing/mode volume of highly enhanced electric field intensity. Two examples of this effect are shown in Figure 23g,h for a single silver nanocube, as calculated by finite difference time domain (FDTD) simulation, and a single gold bipyramid, as calculated by the finite element method (FEM).

There are subtle differences between the bulk refractive index sensitivity of a particle and its molecular detection sensitivity. This distinction will be addressed in depth in a later section, but

Table 2. Summary of Nanoparticle Shapes and Their Refractive Index Sensitivities[a]

			λ_{peak}		$\Delta\lambda$		shift/RIU		
ref	particle	type	nm	eV	nm	eV	nm	eV	FOM
Chen 2008[43]	Au branches	ensemble	1141	1.09	879	0.983	703	0.415	0.8
Tam 2004[46]	Au/SiO_2 shell	ensemble	770	1.61	350	0.732	314	0.657	0.9
Sun 2002[47]	Au/AuS shell	ensemble	700	1.77	400	1.01	409	1.04	1.0
Wang 2006[48]	Au nanorice	ensemble	1600	0.775	600	0.291	801	0.388	1.3
Mayer 2008	Au nanorod	ensemble	720	1.72	125	0.301	170	0.327	1.3
Underwood 1994[49]	Au sphere	ensemble	530	2.34	60	0.265	090	0.397	1.5
Raschke 2004[50]	Au/AuS shell	single	660	1.88	77	0.220	117	0.333	1.5
Sherry 2005[21]	Ag cube	single	510	2.43	91	0.433	146	0.695	1.6
Malinsky 2001[51]	Ag NSL	ensemble	564	2.20	104	0.405	191	0.745	1.8
Nehl 2006[17]	Au star	single	675	1.84	125	0.340	238	0.649	1.9
Lee 2009[52]	Au pyramid	single	680	1.82	114	0.310	221	0.450	2.2
Mock 2003[53]	Ag sphere	single	520	2.38	73	0.335	160	0.734	2.2
Bukasov 2007[54]	Au crescent	ensemble	1795	0.69	209	0.080	596	0.190	2.4
Khalavka 2009[55]	Au rattle	single	570	2.18	52	0.198	199	0.568	3.8
Mock 2003[53]	Ag triangle	single	760	1.63	80	0.172	350	0.751	4.4
Burgin 2008[56]	Au bipyramid	ensemble	681	1.82	52	0.140	352	0.620	4.5
Sherry 2005[21]	Ag cube-sub	single	430	2.88	22	0.146	118	0.792	5.4
Nehl 2006[17]	Au star	single	770	1.61	124	0.260	665	1.41	5.4

[a] Updated from a previous version.[57] This is by no means a complete list but attempts to show a cross-section of the work in this area.

as an example, consider the work of Unger et al., in which an AFM tip is used to maneuver 60 nm dielectric spheres into close proximity to a gold nanocrescent. (See Figure 24.) The LSPR peak shifts by an average of 11 nm when the dielectric sphere is placed in the tip region where the electric field is enhanced.[66] To design optimal particles for biosensing applications, therefore, the particle shape is more important than its effect on the bulk refractive index sensitivity might seemingly indicate.

4.3. Nanoparticle Material

The vast majority of LSPR sensing experiments have been carried out on gold or silver nanoparticles. Gold is often chosen because of its chemical stability and resistance to oxidation, but silver has sharper resonances and higher refractive index sensitivity. A comparison of gold and silver nanoparticles of similar size and shape highlights this fact. For example, for spheres 50−60 nm in diameter, the refractive index sensitivity is 60 nm/RIU for a plasmon resonance at ∼530 nm for gold[47] and 160 nm/RIU for a plasmon resonance at ∼435 nm for silver.[53] As another example, for nanocubes 30−50 nm in size, the refractive index sensitivity is 83 nm/RIU for a plasmon resonance at 538 nm for gold[43] and 146 nm/RIU for a plasmon resonance at 510 nm for silver.[21] (See Figure 25 and Table 3.) In these examples, the effect of the material dominates over the effect of increasing refractive index sensitivity at longer plasmon resonant wavelengths discussed above, so even though the plasmon resonances of silver particles are at lower wavelengths, they are more sensitive than those of gold. This phenomenon is one of the reasons for the significant scatter to the data in Figure 22, which includes both gold and silver nanoparticles.

The reason for the differences in refractive index sensitivity lies in the dielectric functions of the two metals. As discussed in section 2, the location of the plasmon resonance peak of a spherical nanoparticle is determined by the wavelength at which $\varepsilon_1 = -2\varepsilon_m$. The real dielectric function of silver varies with wavelength more than that of gold over the visible light region, especially in the 400−600 nm region where the plasmon resonance lies for reasonable values of the dielectric constant of the medium. (See Figure 2.) (This difference is less pronounced for particles with plasmon resonances at higher wavelengths, where the slopes of the real parts of the dielectric functions of the two

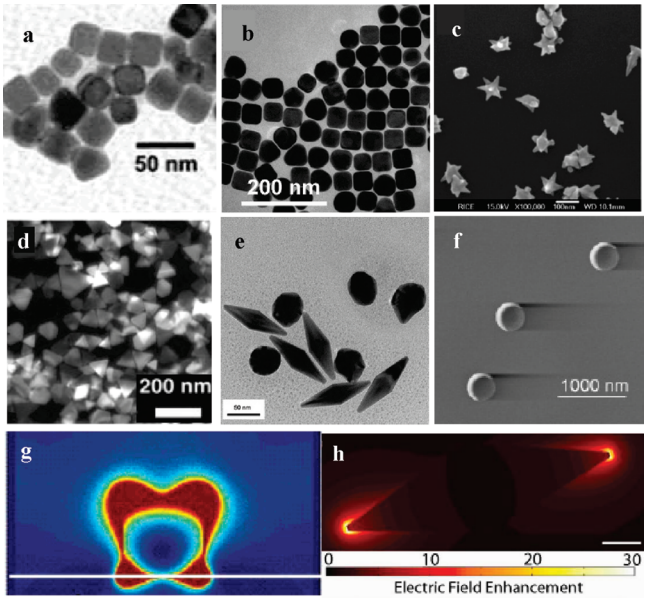

Figure 23. Nanoparticles with corners and sharp tips. (a) Silver nanocubes,[21] (b) gold nanocubes,[43] (c) gold nanostars,[17] (d) silver nanotriangles,[64] (e) gold bipyramids,[60] and (f) gold nanocrescents.[54] Simulated E-field enhancements near (g) a silver nanocube (FDTD)[21] and (h) a gold bipyramid (FEM).[65] Reprinted with permission from refs 17,21,43,54,60,64,65. Copyright 2005−2008 American Chemical Society, 2001 AAAS, 2010 IOP.

dx.doi.org/10.1021/cr100313v |*Chem. Rev.* 2011, 111, 3828–3857

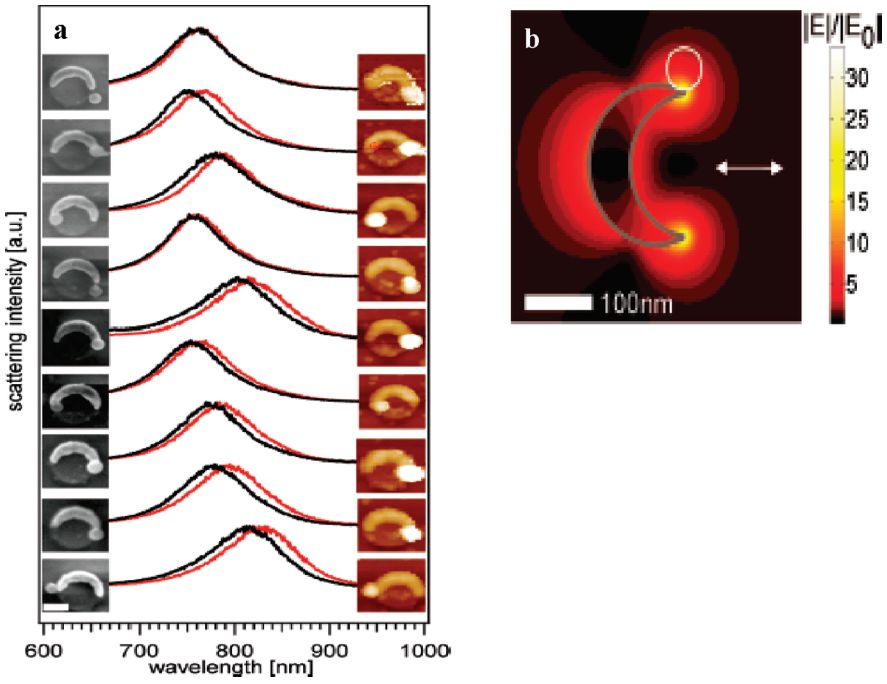

Figure 24. (a) LSPR shift of gold nanocrescents upon attachment of a 60 nm dielectric sphere. (b) E-field enhancement of a gold nanocrescent, showing regions of high enhancement at the sharp tips. Reprinted with permission from refs 66. Copyright 2009 American Chemical Society.

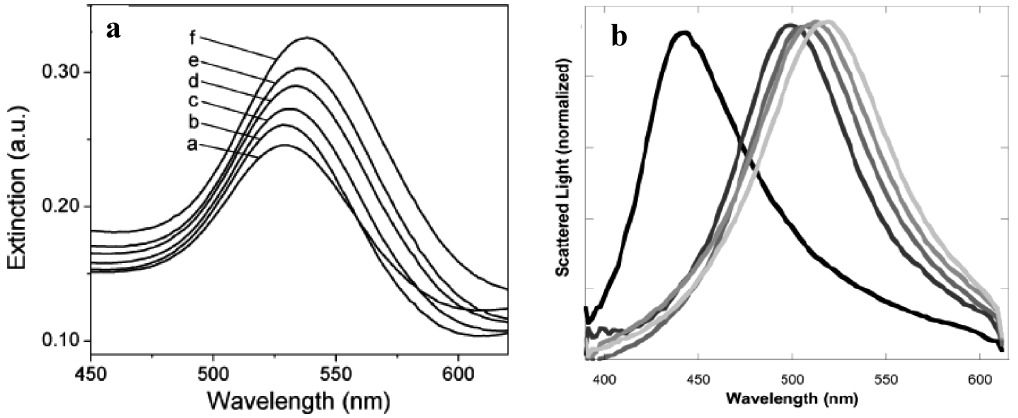

Figure 25. Refractive index sensitivity of (a) gold nanospheres[47] in the refractive index range $n = 1.33-1.50$ and (b) silver nanospheres[53] in the range $n = 1.00-1.56$. These data result in sensitivities of 60 nm/RIU for the gold and 160 nm/RIU for the silver particles. Reprinted with permission from refs 47,53. Copyright 2002, 2003 American Chemical Society.

metals are similar.) Also, because the imaginary part of the dielectric function of silver is less than that of gold across the visible region, less plasmon damping occurs, resulting in higher scattering efficiency and narrower plasmon linewidths.[42] This is a significant advantage in practical sensing applications. For example, for silver and gold nanoparticles with similar refractive index sensitivities, the silver particles are more desirable because they provide a stronger and sharper plasmon resonance curve whose peak wavelength can be more accurately determined. The differences in nanoscale optical properties between silver and gold was shown directly by Link et al. in experiments on nanoparticles of gold−silver alloys of varying composition.[67] The effect of material composition was demonstrated to be much greater than that of particle size, and a linear relationship between plasmon peak wavelength and mole fraction of gold in the alloy was shown. (See Figure 26.)

In addition to silver and gold, plasmonic nanoparticles can be synthesized from other metals. For example, palladium nanocubes, prisms, and plates have plasmon resonances that can be tuned from 330 to 530 nm,[68,69] but their sensing applications have yet to be explored. (See Figure 27.)

4.4. Beyond Nanoparticles

Another category of LSPR sensors is those that depend not on a simple nanoparticle plasmon resonance, but rather on a more complicated extended structure. By exploiting the geometry of nanoparticle arrays and other planar nanostructures, plasmonic extinction spectra with intense, narrow resonances and high

dx.doi.org/10.1021/cr100313v |*Chem. Rev.* 2011, 111, 3828–3857

Table 3. Effect of Material Composition on LSPR of Particles of Similar Shape and Size

particle type	size (nm)	LSPR peak (nm)	sensitivity (nm/RIU)
gold nanospheres	50	530	60
silver nanospheres	60	435	160
gold nanocube	44	538	83
silver nanocube	30	510	146

refractive index sensitivities can be designed. For example, using innovative lithography methods, Henzie et al. have designed multiscale nanohole arrays in gold films with multiple plasmon resonances in the near-infrared region of their transmission spectra.[70] (See Figure 28b.) These resonances are as narrow as 14.5 nm, with refractive index sensitivities of up to 313 nm/RIU. Another example is the periodically perforated metal film structure developed by Liu et al.[71] (See Figure 28a.) In this micrometer-scale structure, interfering bright and dark antenna modes produce a narrow reflectance peak in the infrared region (at 1.76 μm). The refractive index sensitivity of this peak is 588 nm/RIU.

There has also been some interest in the LSPR sensing capabilities of nanostructures exhibiting Fano resonances in their extinction spectra. Fano resonances arise in asymmetrical nanostructures (such as nonconcentric core−shell particles) when a typical, "bright" plasmon mode, which couples to light, interferes with a "dark" plasmon mode, which does not couple to light. The result is a sharp dip in the extinction, which is theoretically predicted to have extremely high refractive index sensitivity.[72]

In addition to optimizing the design of metallic nanostructures themselves, improved refractive index sensing can be achieved through careful design of the substrate supporting the plasmonic structure. Dmitriev et al. have demonstrated the great improvement in refractive index sensitivity that can be introduced simply by raising the metal nanoparticles above the substrate on a dielectric pillar, freeing up the space for solutions to enter more of the region of enhanced electric field intensity. For nanodiscs, this strategy increased the sensitivity by a factor of 2.[73]

4.5. Outlook

While optimizing nanoparticle shape, size, and composition is certainly advantageous, it is not the entire solution to the challenge of extending LSPR applications in science and technology. Other significant issues are the stability and availability of the sensor substrates, their chemical interface with the analyte, and the need for quantitative dynamic measurements. These considerations, and some innovative sensing schemes, will be discussed in more detail in sections 5 and 7.

5. LSPR-BASED BIOLOGICAL SENSORS

Several aspects of LSPR sensing suggest its suitability for biological and biomedical assays. LSPR sensing is label-free. Most assays, such as ELISAs, detect the target antigen after specialized exposure and rinsing protocols, which execute some molecular strategy to generate a signal. In fact, the target antigen is not directly detected in an end point assay, but rather it captures a second antibody, which generates the signal.

In label-free assays, a property of the target antigen molecule itself is detected. This allows a continuous measurement of the target concentration on the sensor and enables the analysis of real-time binding kinetics. Label-free assays are inherently simpler than

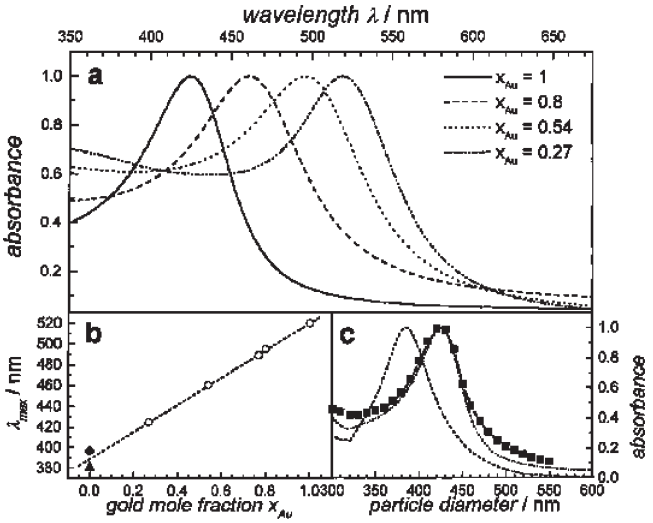

Figure 26. (a) Plasmon resonances of gold−silver alloy nanoparticles. (Note: This legend from the original manuscript is backward.) (b) Linear relationship between gold mole fraction and plasmon absorbance peak. (c) Experimental and simulated spectra of gold−silver alloy nanoparticles. Reprinted with permission from ref 67. Copyright 1999 American Chemical Society.

end-point assays because they require only a single capture antibody and provide direct detection with less extensive protocols. The use of nanoparticle LSPR for label-free assays localizes the sensing area, thus reducing the total amount of analyte needed to generate a signal, and minimizes the effects of diffusion-limited mass transport. However, the lack of amplification in label-free assays inherently limits their sensitivity. For example, Figure 30 displays the saturation signal of an LSPR assay as a function of target concentration, also referred to as a dose−response curve.[74] The signal follows a simple 1:1 binding model in which the detection signal occurs largely at a target concentration near the K_{eq}^{-1} of the capture agent for the target. While the limit of detection will be at some point below this concentration, depending on the signal-to-noise level, the sensitivity is inherently limited by the affinity of the capture agent.

There have been many reports demonstrating biological assays by LSPR sensing and characterizing their performance. Here, we discuss them according to the recognition interaction employed and consider aspects of the measurement that impact sensitivity and other factors.

5.1. Biotin−Streptavidin

The biotin−streptavidin interaction is often measured when developing biological assays because it forms a strong, specific bond, and many reagents for bioconjugate techniques based on biotin-streptavidin are readily available. Biotin−streptavidin is especially well suited to LSPR sensing because biotin, a small organic molecule, can be conjugated to the nanoparticle surface, while the index of refraction of the larger streptavidin protein is detected. There have been many reports of the biotin strepatividn interaction by LSPR assays.[75−90] Reported streptavidin sensitivities range from picomolar to micromolar concentrations. This broadly varying performance arises largely due to variations in the observed K_{eq} of the dose−response curves, which is somewhat unexpected because the affinity, while often dependent upon experimental conditions, should not vary by that many orders of magnitude. In solution, the biotin streptavidin binding

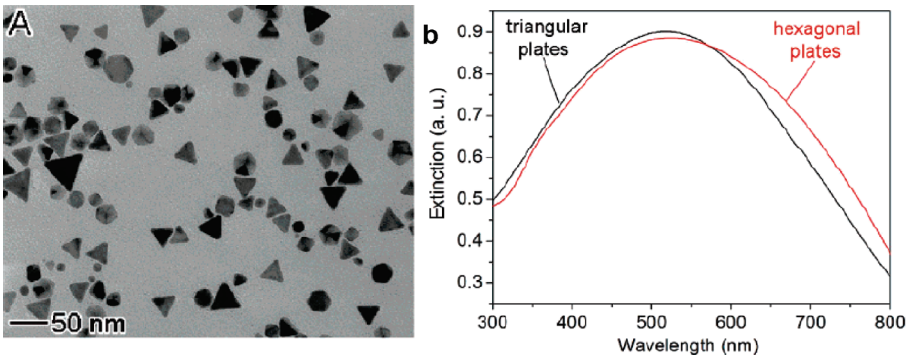

Figure 27. (a) The palladium nanoparticles of Xiong et al. This image shows hexagonal and triangular particles, but one or the other can be produced by controlling the synthesis kinetics. (b) LSPR of the palladium particles. Reprinted with permission from ref 69. Copyright 2005 American Chemical Society.

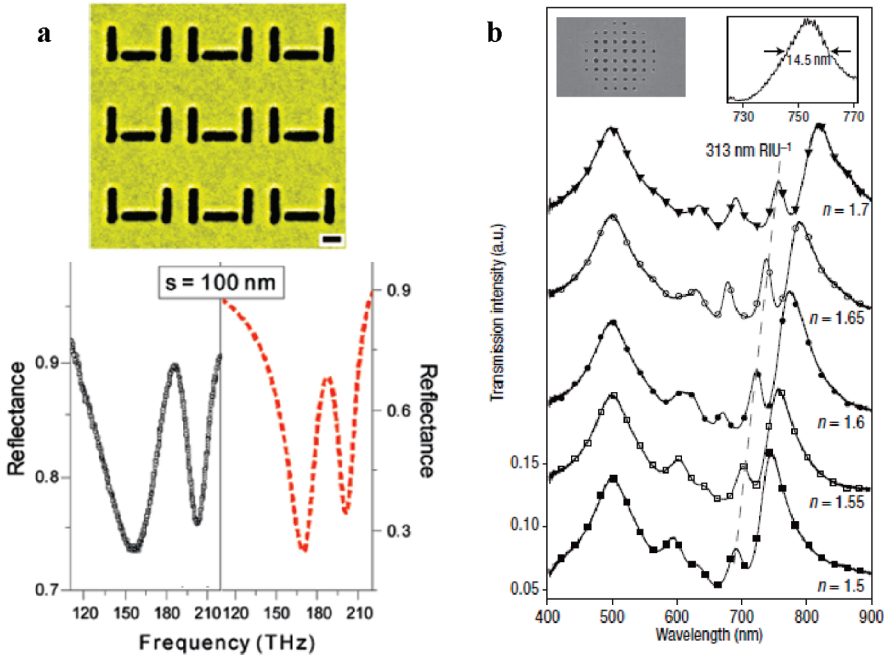

Figure 28. Structures and spectra of two examples of extended plasmonic structures with high refractive index sensitivities: (a) perforated metal film, (b) nanohole array. Reprinted with permission from refs 70,71. Copyright 2007 Nature Publishing Group and 2010 American Chemical Society.

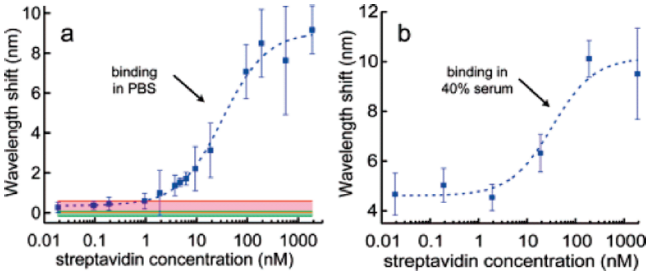

Figure 29. The dose−response curve for streptavidin detection with biotin-functionalized gold nanorods. Reprinted with permission from ref 75. Copyright 2007 American Chemical Society.

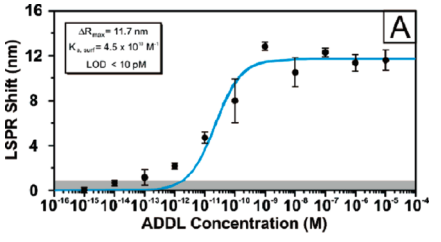

Figure 30. The dose response curve for ADDL against NP-antiADDL. Reprinted with permission from ref 101. Copyright 2005 American Chemical Society.

constant has been found to be on the order of 10^{14} M^{-1},[91] which would lead in principle to femtomolar sensitivities. The reduced affinity that is observed has been attributed to the effects of conjugation of biotin to the nanoparticle surface via a molecular tether, including steric hindrance and limited mobility. The specificity of these measurements is typically demonstrated by a lack of signal upon exposure to nonspecific targets such as bovine serum albumin, antibodies, and biotin-saturated streptavidin. Streptavidin detection has also been demonstrated in serum and dilute blood,[75,82] as seen in Figures 29 and 37.

dx.doi.org/10.1021/cr100313v |*Chem. Rev.* 2011, 111, 3828–3857

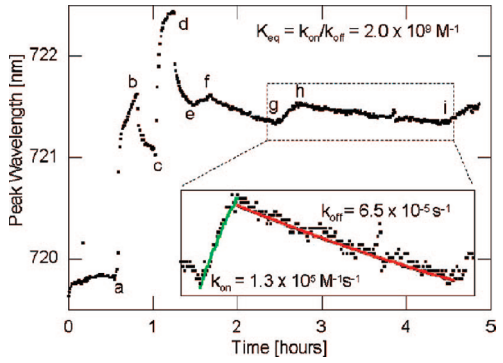

Figure 31. Real-time binding kinetics between antibodies and a specific antigen. Fits to the highlighted portion yield correct kinetic parameters for an antibody−antigen interaction. Reprinted with permission from ref 19. Copyright 2008 American Chemical Society.

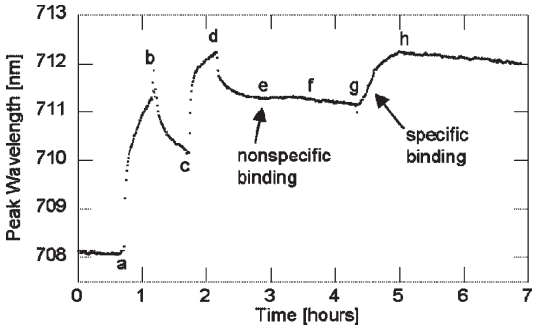

Figure 32. Real-time binding kinetics provide an explicit demonstration of specificity with the response to both nonspecific and specific targets of identical molecular weight and concentration. Reprinted with permission from ref 19. Copyright 2008 American Chemical Society.

5.2. Antibody−Antigen

LSPR sensors have been demonstrated in an immunoassay format.[19,20,65,90,92−109] Capture antibodies are typically conjugated to the nanoparticle surface via a SAM and standard bioconjugate linkers, and most reports characterize the sensitivity based on the dose−response curve. As described above, the sensitivity depends on the binding constant and signal-to-noise ratio. In contrast to the biotin−streptavidin results, some immunoassay reports yield K_{eq}'s that are commensurate with the solution value of 10^9−10^{10} M^{-1}.[19,20,101,106] Figure 30 displays one such dose−response curve for the detection of ADDL, a marker for Alzheimer's disease. It is perhaps not surprising that antibodies would achieve their natural affinity while bound to nanoparticles given their relatively large size as compared to biotin. However, their larger size also increases the separation between the nanoparticle and target antigen, thus lowering the sensitivity and ultimately the limit of detection. Sensitivities are typically found in the picomolar range, but no consistent standard has emerged to evaluate the limit of detection across different LSPR platforms.

Most LSPR assay reports do not describe real-time interaction kinetics, which is a major advantage of label-free assays. The dose−response curves in Figures 29 and 30 are the result of using the LSPR sensor as an end point assay and are useful for comparison to other end point assays. However, to realize the full potential of LSPR assays, the real-time binding kinetics can also be monitored and analyzed. For biotin−streptavidin, this is not practical. The affinity is so strong that the binding kinetics would always be limited by diffusion, and the unbinding kinetics would be hopelessly slow. However, antigen−antibody kinetics are at more reasonable rates and have been studied by other label-free methods such as SPR.[19,20] Figure 31 displays a kinetic analysis of antigen−antibody binding with a gold nanorod LSPR assay. With real-time analysis, initial steps in the conjugation can be monitored, and the binding and unbinding can be repeated within one experiment. The resulting k_{on}, k_{off}, and K_{eq} all match expected values. Furthermore, real-time analysis may be used to demonstrate specificity within a single experiment and over the same nanoparticles. Figure 32 displays the response of an antibody conjugated LSPR sensor as it is exposed to a nonspecific, and then subsequently a specific antigen, both of which were at the same concentration and had the same molecular weight.[19] These observations give a more direct confirmation that antigen−antibody interactions occur on the sensor than do dose response studies, and may be used for interaction analysis.

It is important to note that this type of first-order kinetics measurement can only be obtained in experimental regimes in which the binding kinetics is not dominated by diffusion effects. If target concentrations are too low, the system will exhibit diffusion limited kinetics, and the measured association rate will be slower than the first-order binding. This latter situation is exacerbated in the case of very small sample volumes, in which only a few molecules may be present. The mass transport of molecules in a flow cell from the solution to a surface is described by:[110]

$$J = kCD^{2/3}u^{1/3} \tag{29}$$

Here, J is the diffusion flux in dimensions of $(mol/m^2 \cdot s)$, k is a constant based on the geometry of the flow cell, C is the concentration of the analyte molecule, D is the diffusion coefficient of the solution, and u is the flow rate. If the diffusion flux is much slower than the first-order association rate of the analyte with the capture antibody, the kinetics will be diffusion-limited. Diffusion concerns are a significant issue in the case of SPR kinetics studies, in which the capture antibody must be immobilized in a polymer matrix, rather than simply affixed to a surface. In these experiments, extremely high flow rates must be used to balance the low diffusion coefficient of the matrix.

5.3. Other Biomolecular Interactions

In addition to biotin−streptavidin and antibody−antigen interactions, LSPR sensing has been used to probe other biomolecular interactions, including nucleic acid hybridization and protein−carbohydrate, cytochrome−inhibitor, aptamer−-protein, and toxin−receptor interactions. Also, some LSPR bioassays have been carried out in complex fluids such as serum and whole blood.

Yoo et al. have used spectra from a multispot LSPR substrate based on a gold-capped nanoparticle array (as described in section 7.1 on multiplexing) for label-free measurements of DNA hybridization.[111] They studied mutations of the BIGH3 gene (Figure 33), which are associated with corneal dystrophy, detecting four variants of the gene with single point mutations, with a detection limit as low as 1 pM. Target DNA segments of different lengths were tested, with segments of 147 base pairs having the best detectivity. The mutations were also successfully detected in actual patient samples, which were heterozygous with both normal and mutant variants of the gene present.

In the area of protein−carbohydrate interactions, LSPR sensing has been used to study the binding of concanavalin A (ConA), a type of lectin occurring in plants. ConA preferentially

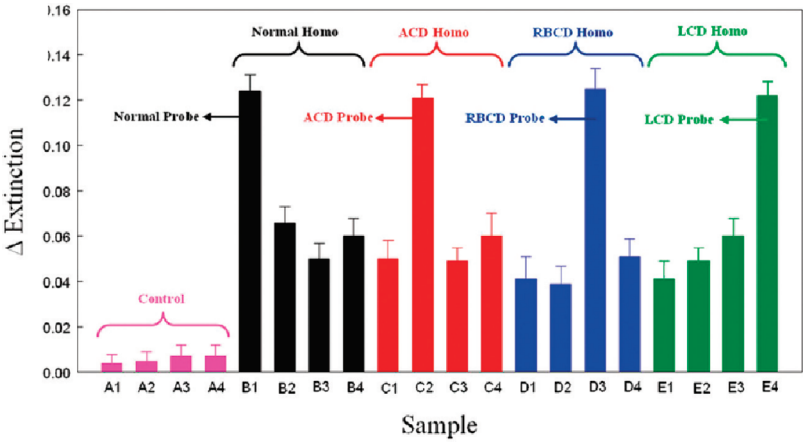

Figure 33. Detection of BIGH3 gene variants by Yoo et al. Sensor response to four target DNA sequences varying by only one base. Reprinted with permission from ref 111. Copyright 2010 American Chemical Society.

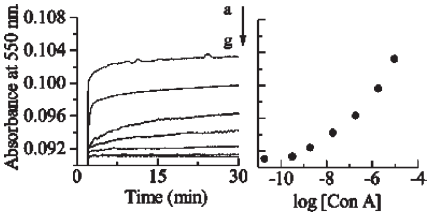

Figure 34. Concentration-dependent response of the glucose-based ConA sensor of Morokoshi et al. Reprinted with permission from ref 112. Copyright 2004 American Chemical Society.

binds to the sugar mannose and also binds to certain residues in other sugars. Yonzon et al. demonstrated LSPR sensing of ConA by silver nanotriangles functionalized with mannose. A high target concentration was used (19 μM), but good specificity and real-time kinetics were shown. (This work is discussed in more detail in sections 3.3 and 7.1.) Around the same time, Morokoshi et al. developed a method for functionalizing gold nanospheres with glucose-bearing polymer chains.[112] They then studied the binding of ConA to glucose via LSPR sensing and measured the kinetics over 6 orders of magnitude of target concentration, with a limit of detection of 1.9 nM. (See Figure 34.) They also showed that when mannose, which binds ConA more strongly than glucose, is added to the solution, they do not detect ConA.

Another type of biomolecular interaction that has been studied by LSPR sensing is the binding of a small drug molecule (either a substrate or an inhibitor) to cytochrome. These studies were based on the method of LSPR sensing near molecular resonances developed by Haes et al., in which the LSPR shift experienced by metal nanoparticles upon coating with a molecule is greater when the LSPR peak wavelength matches the optical absorbance of the molecule.[113] In the cytochrome experiments by Zhao et al., silver nanotriangles were functionalized with cytochrome P450, a heme protein important in drug metabolism and hormone synthesis. The cytochrome molecule has absorption bands in the visible range that blue-shift upon the binding of camphor (a substrate) and red-shift upon the binding of imidazole (an inhibitor). Because these absorption bands overlap the particles' LSPR, a concomitant blue- or red-shift in the nanoparticle extinction is seen in Figure 35, 3−5 times larger than the refractive index shift produced by the same small molecules.[114]

Das et al. went on to apply the technique to cytochrome P450 3A4, the membrane-bound variant of the protein.[115] In this case, silver nanoparticles were functionalized with assemblies consisting of the cytochrome molecule incorporated into a nanodisc, a 10 nm-diameter lipid bilayer disk encircled by scaffold proteins. The cytochrome−nanodisc assembly had absorption bands similar to the nonmembrane-bound form, allowing LSPR sensing to be carried out in much the same way. The response to three different drugs was measured, and the researchers detected a large red shift in the case of ketoconazole, a large blue shift in the case of testosterone, and a negligible shift in the case of erythromycin.

In another example of the use of LSPR sensing for membrane-based systems, Galush et al. incorporated silver nanocubes into supported lipid bilayers by functionalizing the nanoparticles with an alkanethiol SAM, which formed a hybrid bilayer with phospholipid molecules. The authors used the ensemble scattering of the nanocubes to monitor binding of neutravidin to membrane-bound biotin, as well as binding of yellow fluorescent protein (YFP) to functionalized lipid molecules. In the latter case, real-time measurements were taken and the unbinding rate of YFP was compared well to that measured by fluorescence microscopy.[116]

LSPR biosensing has also been applied to the problem of inhibition of acetylcholinesterase (AChE), an enzyme important in nerve function, by an organophosphorous pesticide (paraoxon).[117] In this study, gold nanospheres were deposited on an unclad section of an optical fiber (similar to the strategies described in section 7.3) and functionalized with AChE. Paraoxon was then detected over a range of concentrations, with a limit of detection of 0.234 ppb.

Li et al. have designed gold nanorod-based LSPR sensors for the detection of small, biologically relevant dithiol molecules including glutathione and cysteine.[118] In this work, gold nanorods coated with PEG-thiol (polyethylene glycol) were exposed to four different dithiols in aqueous solution. The sensor response was measured as the change in differential extinction at the wavelength of maximum initial differential extinction. As seen in Figure 36, the smallest molecule, cysteine, led to the largest plasmon shift; the authors attribute this to the reduced steric hindrance between the PEG and dithiol molecules, as the dithiol binds directly to the gold surface.

An innovative LSPR biosensing strategy incorporating both antibodies and RNA aptamers was described by Hiep et al. Aptamers are short (~20 bases) sequences of single-stranded

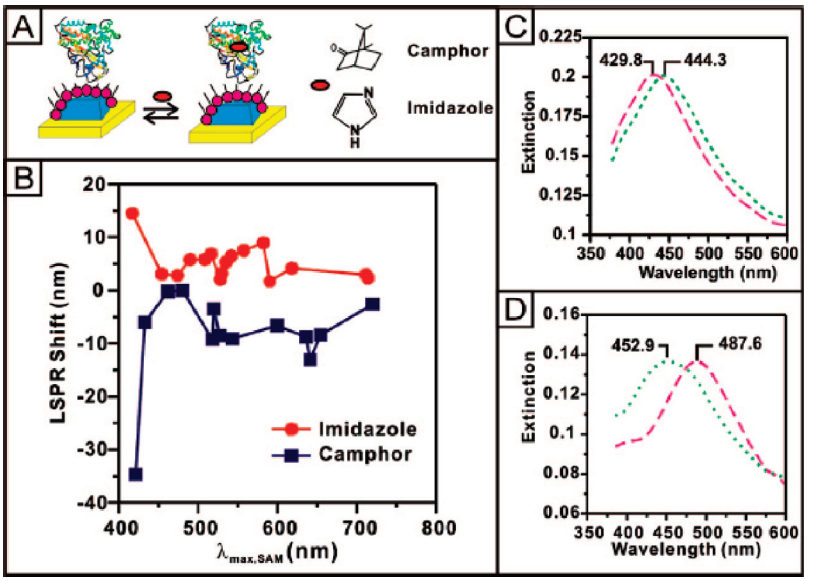

Figure 35. LSPR sensing near molecular resonance of cytochrome (Zhao et al.). Reprinted with permission from ref 114. Copyright 2008 American Chemical Society.

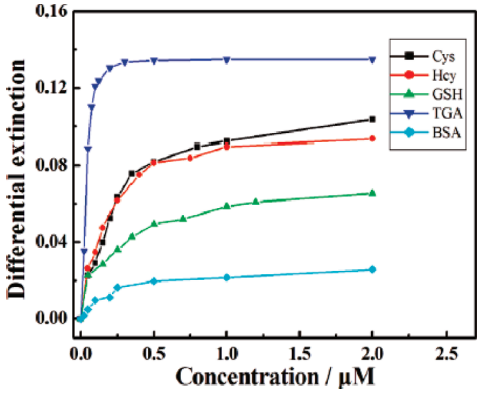

Figure 36. Response of the LSPR sensor of Li et al. to varying concentrations of small, biologically relevant dithiols: cysteine (black), homocysteine (red), glutathione (green); and for comparison, BSA (cyan) and thioglycolic acid (blue). Reprinted with permission from ref 118. Copyright 2010 American Chemical Society.

DNA or RNA with a high affinity for a specific protein molecule; thus, they can be thought of as artificial antibodies.[119] Aptamers have already been applied as a recognition agent in SPR.[120,121] In this assay, antifibrinogen antibodies were linked to a gold-capped nanoparticle substrate via an RNA apatamer, and fibrinogen was detected. Using an aptamer in this way allows for control over the orientation of the capture antibody on the nanoparticle surface, as the aptamer binds specifically to the antibody's Fc domain. The authors of this study detected both the aptamer−protein and antibody−antigen binding steps, with a limit of detection of 0.1 ng/mL for fibrinogen. Cho et al. have also demonstrated a novel molecular detection mechanism based on aptamers linked to gold nanoparticles; however, their approach was based on SERRS (surface enhanced resonance Raman spectroscopy) and not plasmon resonance sensing.[122] In future LSPR studies, using aptamers not as a linker, but as a recognition element to be used in place of antibodies, would be advantageous. Unlike an antibody-functionalized substrate, an aptamer-functionalized substrate is quite robust and can be regenerated many times by rinsing in concentrated salt solution to remove bound target. Another advantage of aptamer-functionalized substrates is that the capture layer is much thinner than for antibodies, bringing the target molecules closer in to the nanoparticle sensing volume. However, aptamer-based strategies currently have some significant limitations. The current screening methods for discovering aptamers are tedious, and until more automated methods are widely adopted, the number of specific aptamers available will remain low.[123] In addition, aptamers are not useable in media where nucleases may be present.

If LSPR sensors are ever to be used in medical diagnostics, they must be able to function on complex fluids such as blood; this will be discussed further in section 9. One such demonstration, by Wang et al., has already been carried out. They achieved detection of streptavidin in diluted (20%) whole blood using films of biotin-coated gold nanoshells.[82] (See Figure 37.) The nanoshell LSPR was in the near-infrared, where blood is relatively transparent. Biotin−streptavidin binding was measured through changes in the absorption intensity at 730 nm, with a limit of detection of 3 μg/mL of streptavidin.

6. LSPR-BASED CHEMICAL SENSORS

6.1. Gas Sensors

Because LSPR sensors are rapid and label-free, there has been a great deal of interest in developing not just biological, but chemical sensing applications of this technology. In particular, a variety of LSPR sensing schemes have been developed for organic vapors. Cheng et al. have demonstrated LSPR sensing of volatile organic compounds (VOCs, e.g. toluene) in gaseous form.[124] In their initial studies, the adsorption of these compounds to substrate-bound silver and gold nanoparticles and gold nanoshells was monitored through both the peak wavelength and the integrated total magnitude of the particles' extinction. The response was fast and reversible. The limit of detection for toluene was 5 ppm in this nonspecific refractive index sensing scheme.

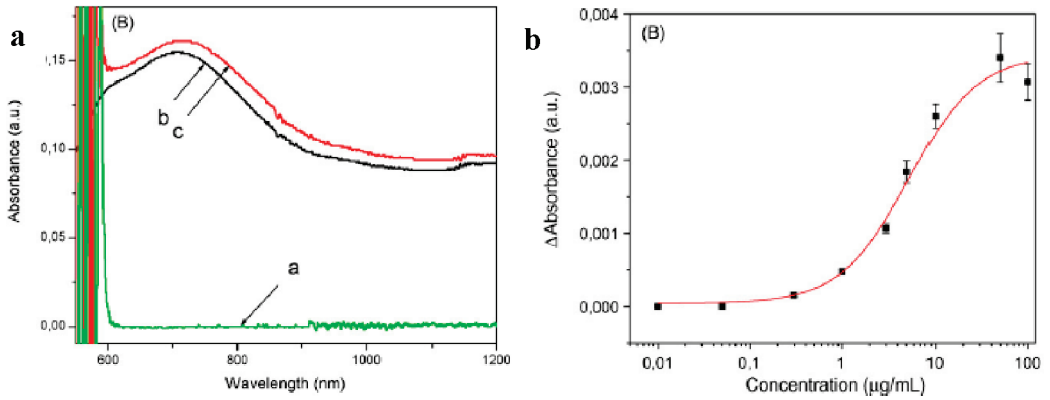

Figure 37. Detection of streptavidin in diluted whole blood by Wang et al. (a) Absorbance of diluted whole blood (green), gold nanoshells in buffer (black), and gold nanoshells in diluted whole blood (red). (b) Dose response for varying streptavidin concentration. Reprinted with permission from ref 82. Copyright 2008 Elsevier.

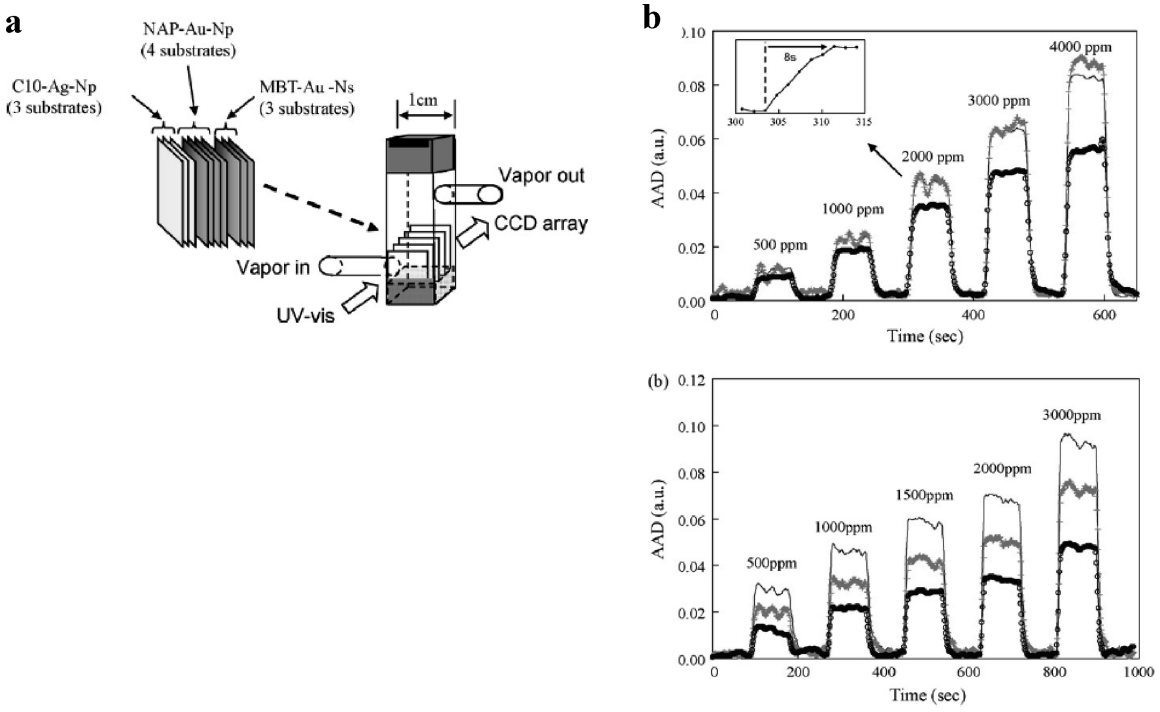

Figure 38. (a) Scheme of the nine-gas sensor of Chen et al. (b) Using the sensor to differentiate between xylene (top) and pentanol (bottom). Reprinted with permission from ref 125. Copyright 2010 Elsevier.

The same researchers later reported a specific, multiplexed sensor, in which three particle types were functionalized with three different self-assembled monolayers (SAMs) with varying affinities for the different organic targets. (See Figure 38.) Using a scheme of stacked substrates, they detected nine different gases with mutually differentiable response patterns, with limits of detection as low as 16 ppm.[125] (The SAMs endow the sensor with specificity at the expense of some detection sensitivity, as the target is moved further from the surface.)

Another scheme for LSPR-based gas sensing was developed by Karakouz et al., in which evaporated gold island films were coated with the polymers polystyrene sulfonic acid (PSS) and polystyrene (PS). These polymers swell and/or shrink upon exposure to the various gases used (chloroform, water vapor, etc.), affecting the local refractive index and inducing LSPR peak shifts. (See Figure 39.) The limit of detection of this method was reported in terms of the vapor pressure of the gas: $0.05P_{sat}$.[126]

6.2. pH Sensors

Plasmonic nanoparticles, usually in combination with pH-sensitive polymers, have also been used in a variety of pH sensing schemes. For example, Nuopponen et al. have designed a pH sensor based upon gold nanospheres coated with the pH-sensitive block copolymer poly(methacrylic acid)-*block*-poly(*N*-isopropylacrylamide) (PMAA-*b*-PNIPAM). The polymer-coated particles were suspended in an aqueous solution and formed aggregates in a pH-dependent manner between pH 5 and 8. However, the process is also temperature dependent, and the particle agglomeration is irreversible.[127]

Later, Mack et al. reported a plasmonic crystal-based pH sensor.[128] The plasmonic crystal consisted of a gold film over a

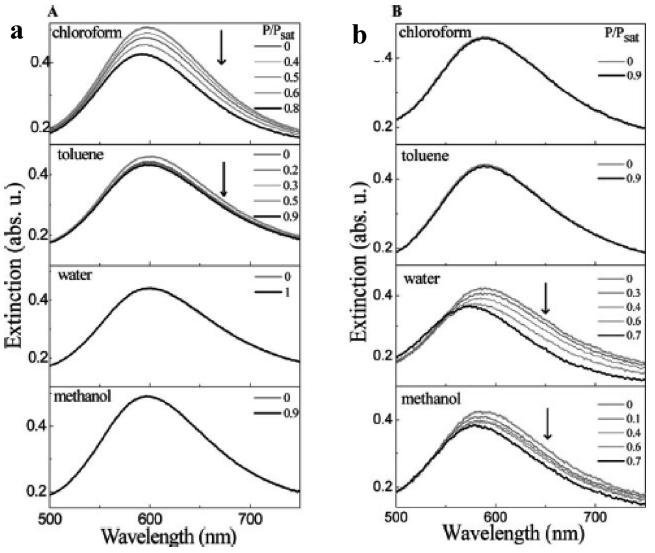

Figure 39. Spectral response of the vapor sensor of Karakouz et al. based upon gold island films coated with (a) PS and (b) PSS. Reprinted with permission from ref 126. Copyright 2008 American Chemical Society.

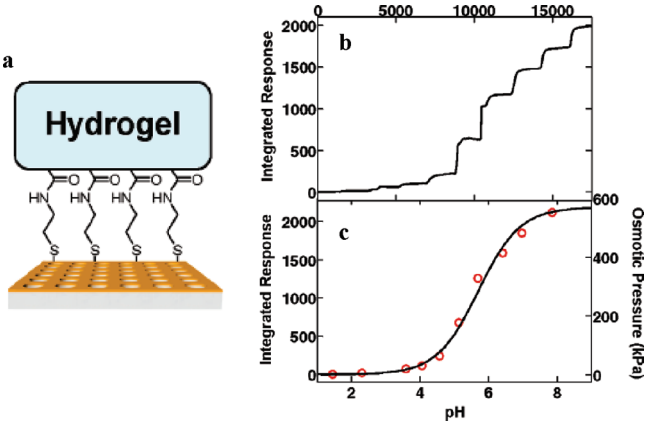

Figure 40. (a) The hydrogel-modified plasmonic crystal pH sensor of Mack et al. (b) Integrated transmitted intensity response to pH. (c) Calculated osmotic pressure experienced by the hydrogel at each pH value. Reprinted with permission from ref 128. Copyright 2007 American Chemical Society.

patterned polymer layer with 480 nm nanowell features. The substrate was then coated with a hydrogel made up of 2.0 wt % acrylic acid (AA), 1.1 wt % ethylene glycol dimethacrylate (EGDMA) cross-linker, 3.7 wt % photoinitiator (PI), 55.5 wt % hydroxyethyl methacrylate (HEMA), and aqueous Brij 58 surfactant. This hydrogel swelled with increasing pH, lowering its density and causing a decrease in refractive index and blue shifts in the multiple LSPR peaks in the transmission spectrum. This mechanism is effective over a pH range of 1.44−7.86. (See Figure 40.) The pH measurement is based on the integrated intensity of the transmission rather than a peak wavelength. The method yields a precision of 0.1 pH unit, although the authors speculate that, based on the noise level, precision of 0.0001 pH unit should be possible. Because this approach is substrate-based and does not rely on aggregation, the sensing mechanism is reversible.

In a related, nanoparticle-based approach, Jiang et al. reported a pH sensor based upon randomly oriented, substrate-bound gold nanocrescents synthesized by a novel lithography method and coated with a pH-sensitive poly(2-hydroxylethyl methacrylate)-based (poly-HEMA) hydrogel.[129] This sensor operates by the same mechanism described above and is effective over a pH range of 4.5−6.4. (See Figure 41.) The sensor is precise to within 0.045 pH unit, and the hydrogel-coated substrates are quite stable, giving repeatable results after 1 month of storage.

6.3. Other

LSPR sensing has also been used to detect aqueous ammonia. In a method developed by Dubas et al., silver nanoparticles are synthesized under UV light in the presence of poly(methacrylic acid) (PMA).[130] The particles produced by this method experience an LSPR shift and concomitant color change upon the addition of ammonia, attributable to the exchange of silver between the silver nanoparticles and $Ag(NH_3)_2^+$ ions in solution, leading to a size and/or shape change in the particles. The LSPR spectrum appears to have two peaks, one near 520 nm, which decreases in height with the addition of ammonia, and one near 415 nm, which increases. This mechanism acts as a colorimetric sensor for ammonia at concentrations ranging from 5 to 100 ppm. (See Figure 42.)

A nanoparticle-based sensor for copper ions based upon plasmonic resonance energy transfer (PRET) was developed by Choi et al.[131] In this scheme, gold nanoparticles were coated with specific ligands that form complexes with copper ion. These were chosen such that the electronic absorption of the metal−ligand complex matched the plasmon resonance of the nanoparticles. This resulted in a quenching of nanoparticle scattering upon copper ion binding for concentrations as low as 1 nM.

Finally, He et al. have developed a combined fluorometric and colorimetric sensor for copper ions, based on gold nanospheres functionalized with the perylene bisimide chromophore.[132] In the presence of copper ion, the dye is freed from the gold nanoparticle surface, reducing quenching and increasing fluorescence intensity. At the same time, the absorbance of the sample increases and red-shifts due to the uncoupling of the nanoparticle and chromophore absorbances. While not strictly an LSPR sensor, this is an intriguing use of plasmonic nanoparticles in a sensing application.

7. TECHNOLOGICAL ADVANCES IN LSPR SENSING

7.1. Multiplexing

Before LSPR sensors can become high-throughput laboratory and clinical screening tools to compete with ELISA and other common assays, the technique must be parallelized to handle large numbers of samples. In an exciting demonstration of the potential of this technology, Endo et al. deposited an array of 300 spots of nanoliter volumes of antibody solutions on a film of gold-capped nanospheres and used a scanning optical probe to measure the optical absorbance of the film to compare the affinity of each antibody for the analyte.[133] (See Figure 43.) The change in integrated absorbance was measured rather than an LSPR peak shift. Antigens were detected at concentrations as low as 100 pg/mL.

Yu, Wang et al. have developed an unconventional approach for multiplexed LSPR sensing using gold nanorods with a variety of aspect ratios.[93,134,135] This approach allows for many fewer parallelizable channels than the above, but has the advantage of requiring no specialized instrumentation. By using nanorods of three different aspect ratios, the channels are separated in terms

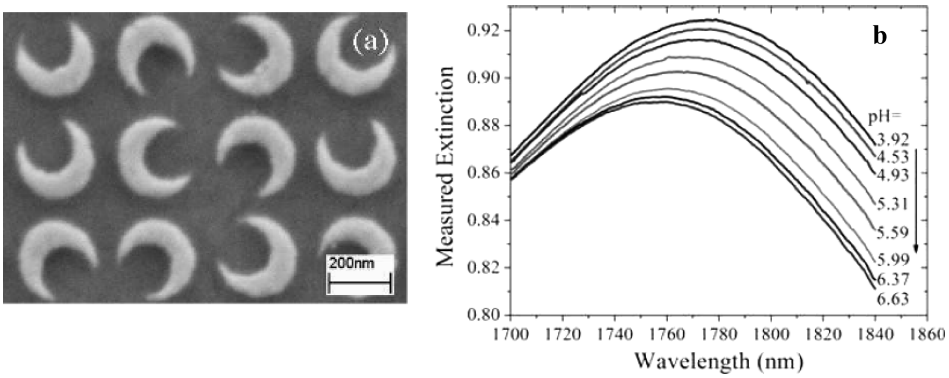

Figure 41. (a) Gold nanocrescent substrate used in the pH sensor of Jiang et al. (b) pH response of the substrate IR extinction spectrum. Reprinted with permission from ref 129. Copyright 2009 Optical Society of America.

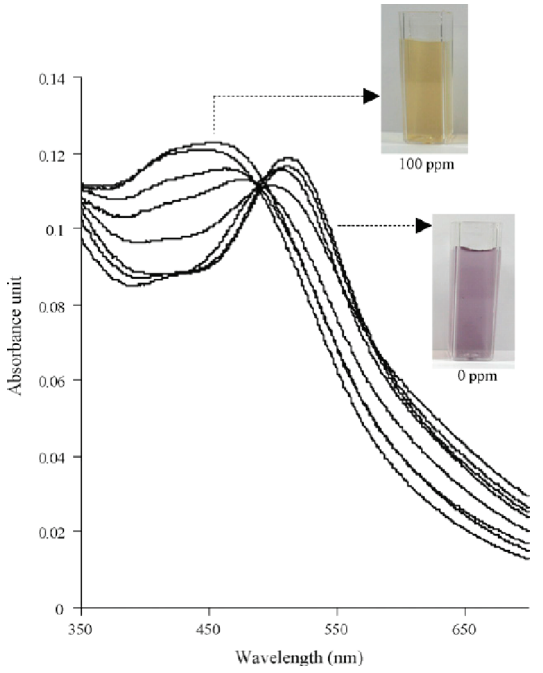

Figure 42. Spectral and color change of silver nanoparticles upon ammonia exposure as described by Dubas et al. Reprinted with permission from ref 130. Copyright 2008 Elsevier.

of LSPR wavelength, so they do not have to be separated spatially to be addressed individually. The authors first demonstrated simultaneous detection of three different antibodies in a buffer solution[93] (see Figure 44), and then went on to adapt the technique to detect three cell surface markers and profile the phenotypes of cells.[134] Finally, they have adapted this spectrally multiplexed nanorod sensor to simultaneously detect *E. coli* and salmonella for food safety applications.[135]

In a similar strategy using silver particles rather than gold, Yonzon et al. demonstrated a duplexed sensor incorporating patterned nanotriangles of two different heights with plasmon resonances at 683 and 725 nm.[34,136] In this case, the particles were fabricated on-chip in two different regions, which were then modified with the sugars mannose and galactose, and exposed to Concanavalin A (ConA). (ConA binds selectively to mannose, but not to galactose.) The LSPR peak shifts of the two particle types could then be monitored simultaneously from the total extinction spectrum of the chip. (See Figure 45.)

In a completely different approach, Bingham et al. reported a method for acquiring multiplexed data from many individual nanoparticles on a substrate in a dark-field microscope.[137] (See Figure 46.) The method relies on a liquid crystal tunable filter (LCTF),[138] which can tune the illumination wavelength from 400 to 720 nm. The entire substrate is imaged many times as the illumination wavelength is scanned. Multiple regions of interest can be selected, and spectra of each particle can be constructed from the scattered intensities at each illumination wavelength. The technique has not yet been applied to LSPR sensing, but is very promising for this purpose.

7.2. Integration with Microfluidics

For LSPR sensors to become practical for use with clinical samples, they must be able to detect targets in very small sample volumes. High speed and high throughput are also desirable. The most common approach to this problem is to use microfluidics, and there has been some promising early work on integrating LSPR sensing and microfluidic systems. Hiep et al. have designed an LSPR chip integrated with a single microfluidic channel, which uses a sample volume of 1 μL. The LSPR substrate itself is a film of gold-capped nanospheres over a flat gold film.[139] (See Figure 47a.) This chip was used to demonstrate bulk refractive index sensing of glucose solutions as well as specific immunodetection of insulin with real-time kinetics and a limit of detection of 100 ng/mL.

More recently, Huang et al. have demonstrated a similar LSPR-microfluidic chip based on films of gold nanospheres.[140] (See Figure 47b.) This scheme had an automated sampling system, two parallel microfluidic channels, and used a sample volume of 2.5 μL. The sensor was demonstrated to measure refractive index to a precision of 10^{-4} RIU. Biotin/antibiotin binding was also measured as a demonstration of immunosensing with this device. Both of these microfluidic chips used simple UV−vis absorbance spectrometers to detect the LSPR signal.

For these microfluidics-integrated LSPR substrates to be scaled up further, strategies to read out the optical extinction from a large number of channels must be employed. One strategy could be to utilize a scanning detector based on a fiber optic probe as in the example in section 7.1, or a scanning sample stage. Another strategy would be to use a variation on the LCTF-based LSPR imaging spectroscopy method described in section 7.1. Instead of individual particles, one could define regions of interest corresponding to patches of the substrate in the different microwells. (This method would be useful for multiplexed

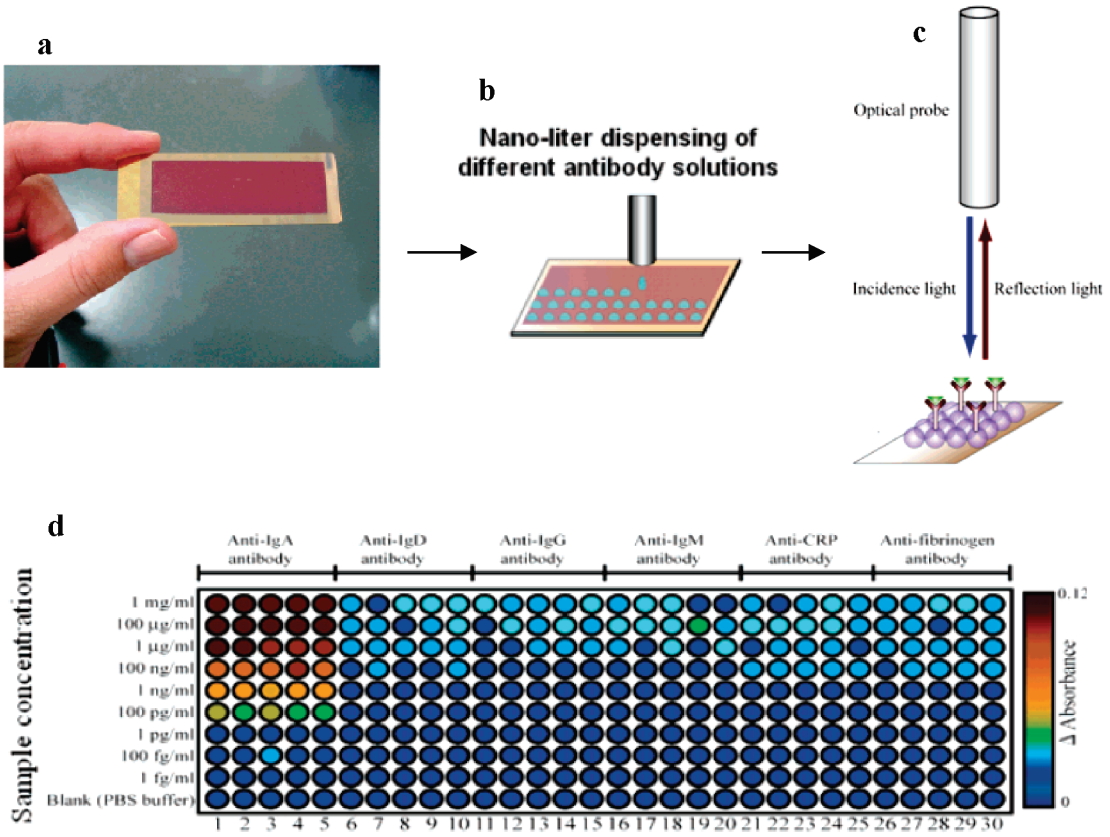

Figure 43. Multiplexed LSPR biosensor of Endo et al. (a) Gold-capped nanosphere film. (b) Array of nanospots is deposited on functionalized substrate. (c) Scanning optical probe. (d) The resulting affinity map for IgA. Reprinted with permission from ref 133. Copyright 2006 American Chemical Society.

measurements in general, with or without microfluidic integration.) Alternatively, depending on the exact substrate response to refractive index changes, the integrated intensity from multiple regions of a CCD image could simply be used instead of spectral data. (As in many of the examples discussed in this section, total intensity rather than peak wavelength changes have been used for LSPR sensing.)

7.3. Optical Fiber Probes

By integrating plasmonic nanoparticles with optical fibers, it may be possible to carry out LSPR sensing in very small volumes, remotely, and even in vivo. Cheng et al. designed a fiber-based LSPR sensor incorporating gold nanospheres adsorbed to the end of the fiber.[141] The LSPR of the particles was observed in the reflectance spectrum measured by the fiber. They demonstrated bulk refractive index sensing, nickel ion sensing, and sensing of biotin−streptavidin binding by this method. Around the same time, Mitsui et al. developed a fiber-based LSPR sensor using only the total reflection intensity of a red light-emitting diode, obviating the need for a white light source and spectrometer.[142] They demonstrated bulk refractive index sensing of water−glycerol mixtures of varying composition, with a precision of 2×10^{-5} RIU (comparable to SPR sensors). They also reported time-dependent measurements of biotin−streptavidin binding.

More recently, Tang et al. reported a modified LSPR sensor based on a long-period fiber grating (LPFG), in which a segment of the optical cladding was removed and gold nanospheres were deposited on the fiber.[143] (See Figure 48.) In this case, due to the coupling of the LSPR-associated evanescent mode of the particles with the optical modes of the fiber, there was a refractive-index sensitive dip in the fiber transmission at IR wavelengths. This device was demonstrated to have high refractive index sensitivity in terms of the transmission minimum wavelength and the intensity. Dinitrophenyl (DNP)/anti-DNP sensing was also carried out with a limit of detection of 0.95 nM, although no kinetics was shown for the antibody−antigen interaction.

In a similar strategy, Shao et al. have reported a sensor in which gold nanospheres are attached to an unclad section of an optical fiber by self-assembly on a polyelectrolyte layer.[144] LSPR sensing is carried out by measuring the total transmission of the fiber. (See Figure 49.) For bulk refractive index sensing, they measured the sensitivity in terms of change in absorbance units per refractive index unit to be as high as 13 AU/RIU. They also demonstrated specific antibody sensing using a well-developed surface functionalization strategy. However, the dose−response curve did not show the expected saturation at high target concentrations. In this scheme, the target molecule is separated from the metal surface by a thick capture layer (see Figure 49, inset), placing the target antibody near the edge of the evanescent wave decay range. It is likely that the capture layer thickness could be reduced, for example, by replacing the polyelectrolyte layer with a thinner SAM, which could improve the target detection. In all of these small-volume fiber-based studies, it is likely that the binding kinetics is limited by diffusion as

dx.doi.org/10.1021/cr100313v |*Chem. Rev.* 2011, 111, 3828–3857

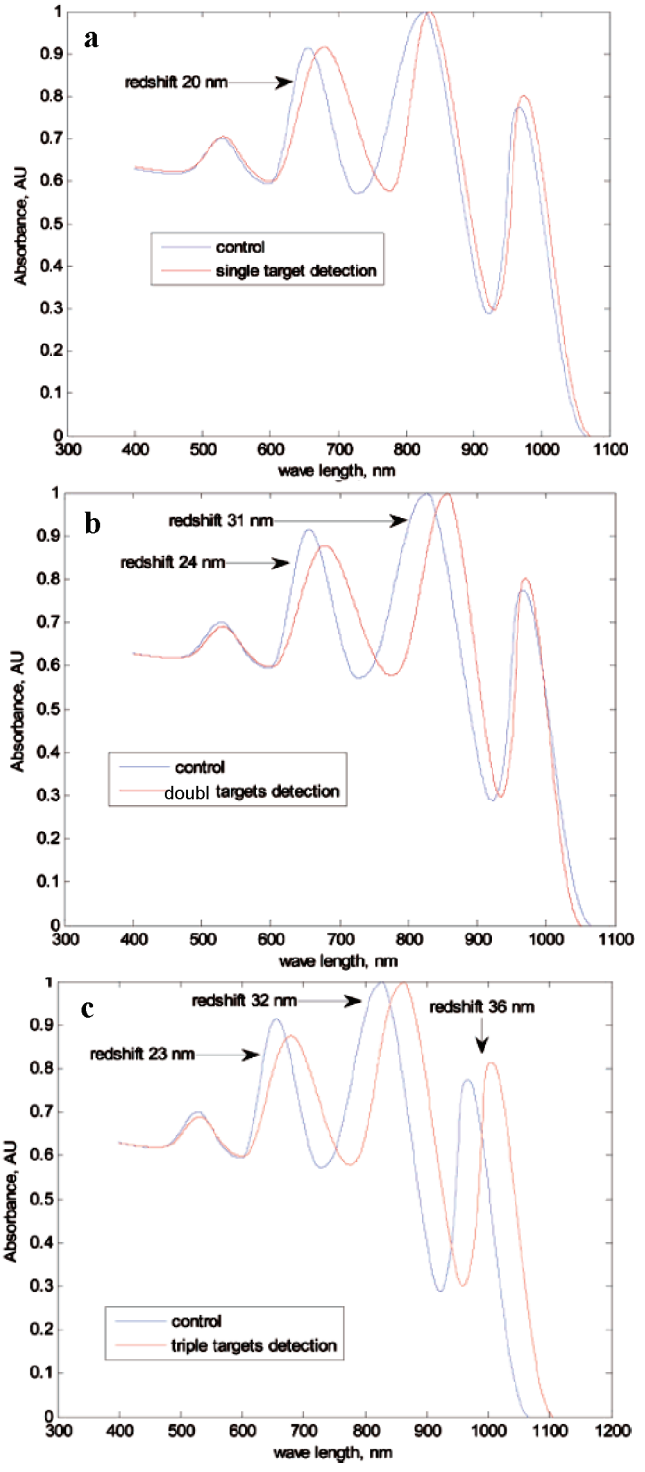

Figure 44. Detection of (a) one, (b) two, and (c) three analytes in a solution containing gold nanorods of three different aspect ratios by Yu et al. Reprinted with permission from ref 93. Copyright 2007 American Chemical Society.

discussed in section 5.2. Therefore, these methods may be useful only as end point assays.

All of the above technological innovations are bringing LSPR closer to a practical sensor technology that could be applied in the lab and/or the clinic. In section 9, we will discuss what has been done, and what is still needed, to make this transition.

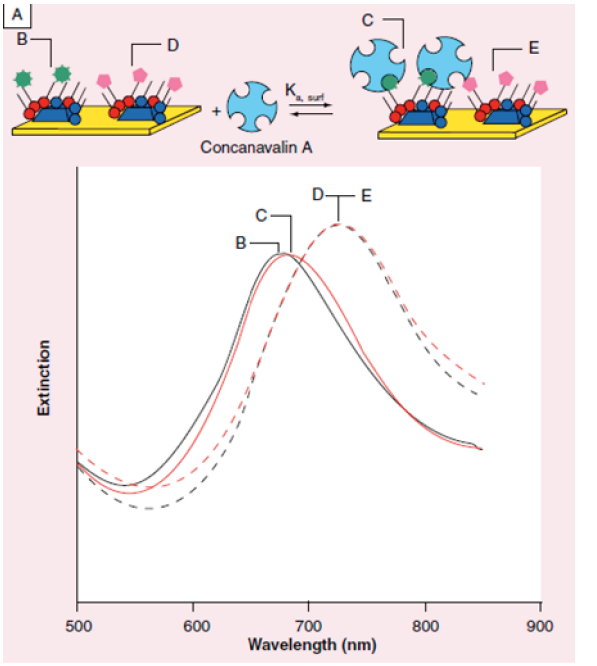

Figure 45. The duplex silver nanoparticle sensor of Yonzon et al. (a) Schematic of the sensor. Silver nanoparticles of two different sizes are functionalized with mannose and galactose. (b) Upon exposure to ConA, only the mannose-coated nanoparticles produce a spectral shift, indicating specific target binding. Reprinted with permission from ref 34. Copyright 2004 American Chemical Society.

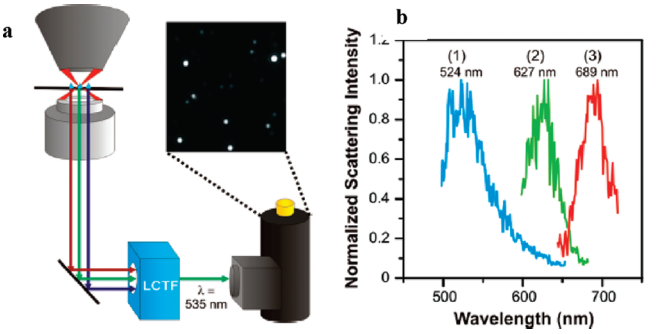

Figure 46. LSPR imaging by Bingham et al. (a) Experimental setup for simultaneous collection of spectra from multiple particles with a liquid crystal tunable filter. (b) Simultaneously acquired spectra of three individual particles. Reprinted with permission from ref 137. Copyright 2009 American Chemical Society.

8. MAXIMIZING THE MOLECULAR DETECTION SENSITIVITY OF LSPR

8.1. Molecular Detection with Single Nanoparticles

As discussed in section 5, LSPR can be the basis for sensing molecular interactions near the nanoparticle surface.[145] That is, one can directly measure molecular binding to a nanoparticle surface through minute changes in the particle's dielectric environment.[146−148] From a qualitative point of view, one can see that the scattering spectra of plasmon resonant nanoparticles can transduce binding of small numbers of molecules. Gold and silver nanoparticles, especially those with elongated geometries, can have high refractive index sensitivities that are localized to

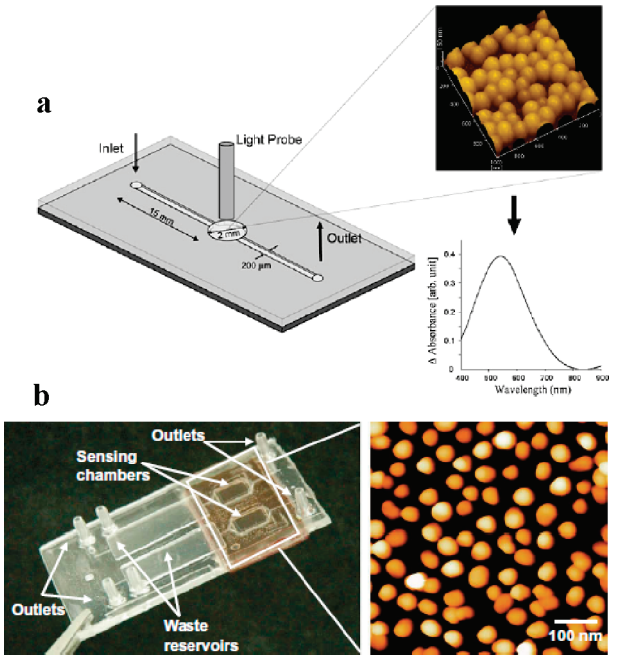

Figure 47. The integrated microfluidic chips of (a) Hiep et al. and (b) Huang et al. Reprinted with permission from refs 139,140. Copyright 2008 Japan Society of Applied Physics and 2009 Elsevier.

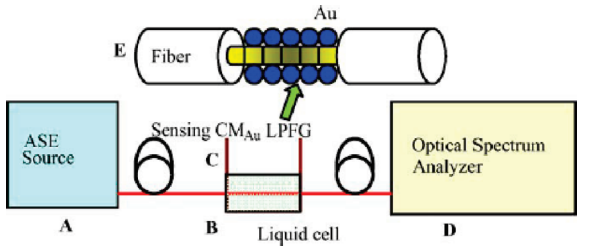

Figure 48. The long-period fiber grating LSPR sensor of Tang et al. Reprinted with permission from ref 143. Copyright 2006 Elsevier.

nanometer-scale sensing volumes surrounding sharp tips.[17,18] If a macromolecule such as a protein with a refractive index different from water enters or leaves this sensing volume, one would expect a discernible shift in the peak wavelength of the plasmon resonance. In past LSPR molecular sensing measurements, sensitivity has gradually increased all of the way up to the detection of individual molecules.[28,65,149−151]

Haes et al. demonstrated LSPR sensing based on the scattering spectra of single silver nanoparticles. The plasmon resonance shift upon the nonspecific adsorption of streptavidin to the metal surface was detected and attributed to approximately 700 streptavidin molecules.[149] (See Figure 50.)

McFarland and Van Duyne also carried out molecular detection experiments for self-assembled monolayers (SAMs) of hexadecanethiol on single silver nanoparticles, measuring shifts due to approximately 60 000 of the small SAM molecules.[152] Around the same time, Rashke et al. carried out similar experiments on single gold nanospheres, with the addition of biotin on the particle surface as a recognition agent for the detection of streptavidin, as described in section 5.[23] Rindzevicius et al. demonstrated LSPR sensing on individual nanoholes in a gold film, using the similar biotin−neutravidin system.[153] Later, this

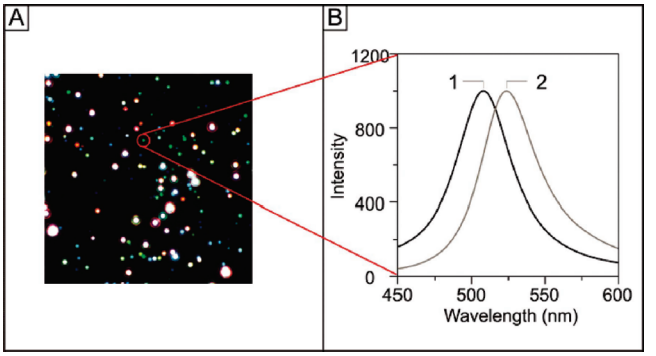

Figure 50. LSPR sensing by single-particle spectroscopy from Haes et al. (a) Dark-field image of silver nanoparticles. (b) Spectral shift upon streptavidin binding to bare silver, attributable to ∼700 molecules. Reprinted with permission from ref 149. Copyright 2004 Springer.

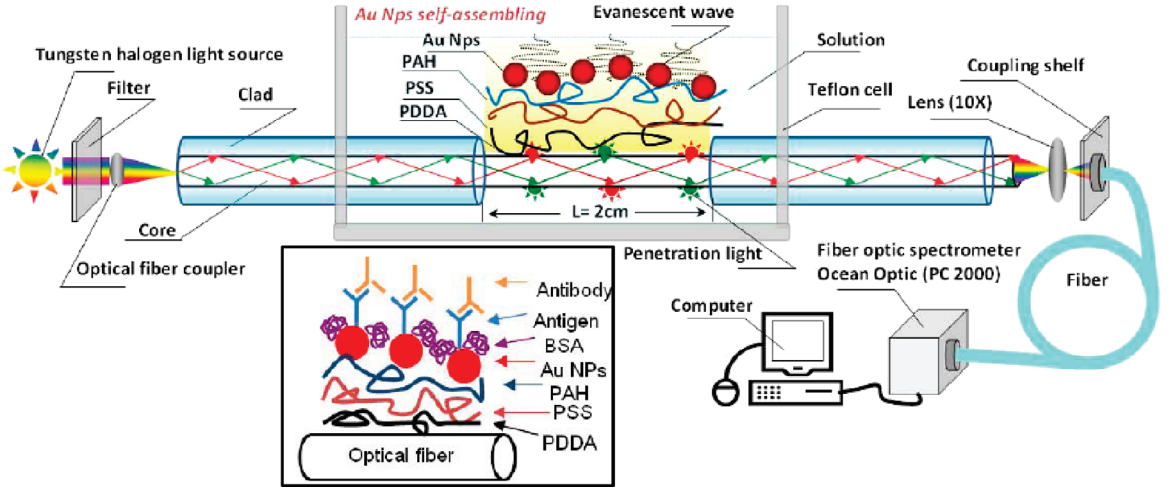

Figure 49. The optical fiber-based LSPR sensor of Shao et al. Inset: Scheme for specific antibody detection. Reprinted with permission from ref 144. Copyright 2010 MDPI.

dx.doi.org/10.1021/cr100313v |*Chem. Rev.* 2011, 111, 3828–3857

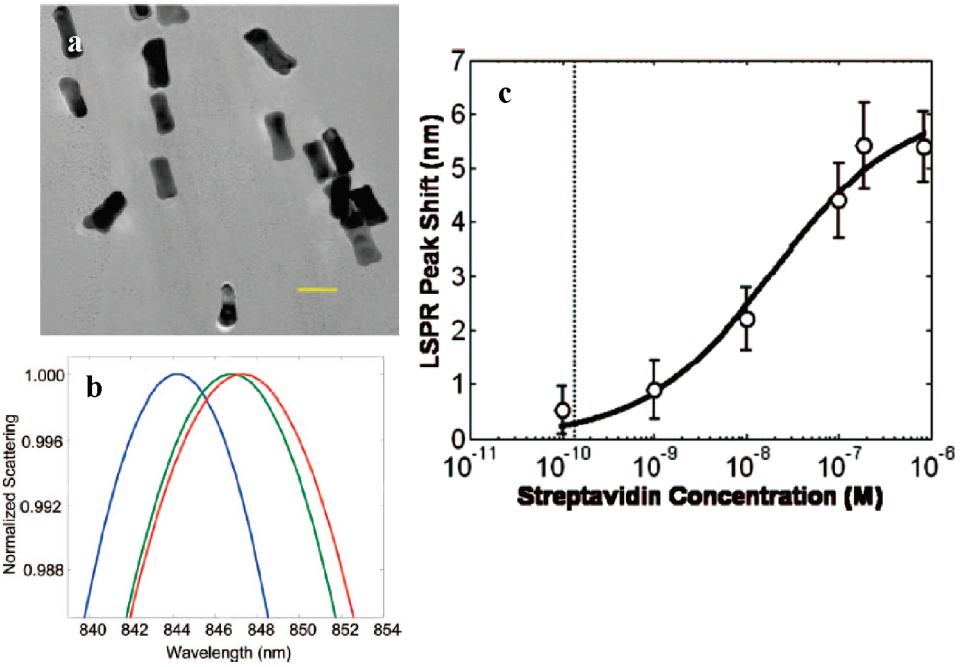

Figure 51. Detection of 18 streptavidin molecules on a single nanorod. (a) Gold nanorods (scale bar equals 50 nm). (b) Fits to spectra in water, with biotin, and after streptavidin binding. (c) Sensitive streptavidin detection (<1 nM). Reprinted with permission from ref 16. Copyright 2008 American Chemical Society.

group carried out molecular detection experiments on ensembles of gold nanorings.[151] Biotin−neutravidin binding was observed in real time, providing kinetics data. The authors discussed their result in terms of the feasibility of few-molecule detection, and it was estimated that the measured LSPR shift was attributable to the binding of approximately 360 neutravidin molecules per nanoring.

Nusz et al. have carried out LSPR biosensing measurements for biotin−streptavidin binding on single gold nanorods. They reported 1 nM streptavidin detection for nanorods 74 nm × 33 nm in size.[16] (See Figure 51). In this study, the LSPR peak wavelength of the nanorods could be resolved to within 0.3 nm. After optimizing the nanorod geometry and developing a model for estimating the molecular detection limit of this sensor, they reported detection of a signal attributable to approximately 18 streptavidin molecules and discussed further refinements that would make single-molecule detection possible.[28] These experiments were carried out with unpolarized light, and the polarization of scattered light was not analyzed. Polarization analysis of single elongated particles can reveal useful structural information, as in the instrumentation described by Wang and Reinhard.[154]

Concurrently, Unger et al. carried out the experiments on dielectric colloids attached to single gold nanocrescents described in section 4.[66] This work offered further support for the idea that single-molecule LSPR sensing should be possible and dramatically illustrated the notion of the localized sensing volumes near particles with sharp tips. On the basis of their calculations and measurements of the peak shift upon colloid binding, the authors calculated that for their system, the binding of a single biomolecule would cause an LSPR peak shift of 0.04 nm, beyond their experimental resolution of 0.3 nm, but they speculated that with improvements to the particle shape and with increase illumination intensity, single-molecule detection ought to be possible. Recently, Mayer et al. achieved single-molecule

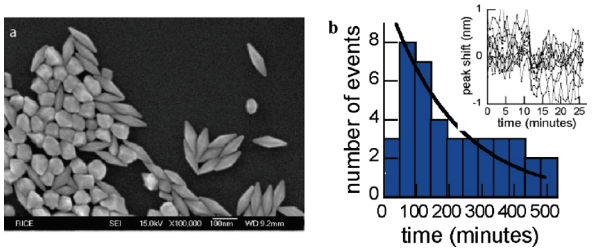

Figure 52. Single-molecule detection by LSPR sensing. (a) Gold bipyramids. (b) Discrete blue shifts in LSPR peak wavelength corresponding to molecules unbinding (inset) and their time distribution. Reprinted with permission from ref 65. Copyright 2010 Institute of Physics.

detection for the dissociation of antibody−antigen pairs on a gold bipyramid. The unbinding of single antibodies resulted in discrete blue shifts of the LSPR peak of 0.34 nm, the timing of which matched the expected dissociation kinetics.[65] (See Figure 52.) These observations were matched by FEM simulations of the plasmon resonance of a gold bipyramid perturbed by a small dielectric sphere. Note that the observed single-particle spectral peak wavelength noise is similar to that of Unger (see above). This was the first label-free detection of single molecules by LSPR shift that included kinetics data.

One of the main challenges in molecular detection by LSPR is now to increase the molecular detection ability of these single-particle systems by improving the signal-to-noise ratio of LSPR peak wavelength shift measurements. Recent work by Käll, Chen et al. has shown an LSPR sensor with a greatly improved resolution of 0.0001 nm in the LSPR peak wavelength.[90] (See Figure 53.) They measured the ensemble extinction of high-quality films of gold nanodiscs prepared by colloid lithography. The strong extinction of these films makes extremely accurate

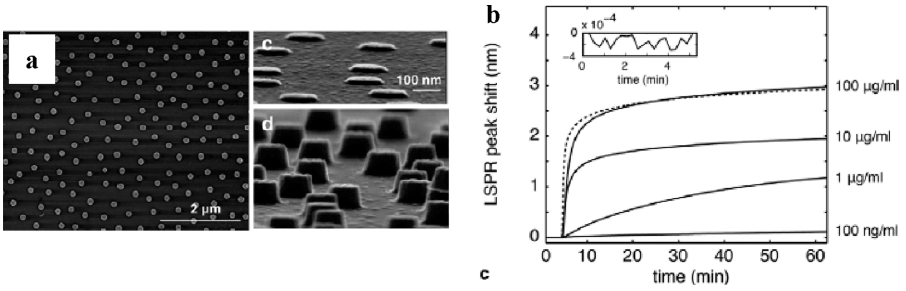

Figure 53. High-resolution nanodisc film LSPR sensor. (a) Structure of the nanodiscs. (b) Low-concentration detection of biotin−streptavidin binding showing the low noise in the LSPR peak wavelength. Reprinted with permission from ref 90. Copyright 2009 Institute of Physics.

peak fitting possible, greatly reducing noise level on measurements of the LSPR peak. This method enabled detection of 30 pM prostate-specific antigen (PSA) on nanodiscs coated with anti-PSA. This was estimated to be equivalent to about 15 molecules per nanoparticle. However, because the improved resolution of this system relies on fitting the spectrum of a dense film with high spectral extinction intensity, it is not extendible to single-particle, single-molecule measurements.

In addition to limitations on the minimum wavelength shift that can be measured, there are other challenges related to single-molecule detection by LSPR. The time resolution of the chosen data collection scheme will impose limits on the types of molecular systems and analyte concentrations such measurements will be useful for. If the analyte concentration is too high, the association rate will be too fast for single-molecule binding events to be resolved. Using a single-wavelength detection scheme would increase time resolution, but at the expense of the LSPR shift resolution that comes with full spectral measurements. If the analyte concentration is too low, the diffusion issues mentioned in section 5.2 will begin to come into play. These factors must be carefully considered in the experimental design of single-molecule LSPR measurements.

8.2. LSPR as a Single-Molecule Method

Single-molecule sensing by LSPR shifts benefits from the noninvasive nature of the measurements. Because the target molecule's refractive index is directly detected optically, there is no need for chemical modification of the target or subsequent binding of other factors to it to generate a signal. Furthermore, unlike in force sensing experiments, the measurements are not taken under any applied load or tension, which are known to affect bond strengths in a load-rate-dependent manner.[155] In single-molecule LSPR experiments, the target molecule is only perturbed by the optical near-field of the nearby nanoparticle.[62]

Label-free optical detection of single molecules has previously been reported based on the effect of heat generated by optically irradiated biomolecules on a microtoroid resonator with a whispering gallery mode (WGM).[156] (See Figure 54.)

The WGM biosensor achieves a high signal-to-noise ratio due to its high quality factor, which greatly exceeds that for LSPR sensors. However, LSPR sensors have the advantages of not requiring microfabrication and the simplicity of the far-field optical readout. Label-free optical detection of single molecules could have a significant impact in several biomedical areas including proteomics, point-of-care diagnostics, and drug discovery.[145,157] LSPR sensing in particular could be a powerful addition to the current toolbox of single-molecule detection methods because it probes interactions on long time scales.

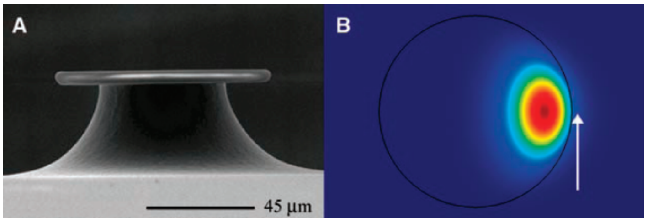

Figure 54. (a) The toroidal microresonator used for label-free single-molecule detection by Armani et al. (b) The optical whispering gallery mode (WGM) of the resonator. Reprinted with permission from ref 156. Copyright 2007 AAAS.

9. FUTURE DIRECTIONS

9.1. LSPR Sensing as a Laboratory Tool for Molecular Biology

On the basis of the comparison in section 3, it is clear that with a few technological improvements, LSPR sensors could become a biomolecular research tool on a par with commercial SPR instruments. Because of the greater simplicity and lower cost of LSPR, one could think of it as "SPR in a cuvette". Yet what is still needed for LSPR sensors to become a viable benchtop instrument? The biggest challenge is sensitivity. The single-particle, single-molecule measurements described in section 8, although maximally sensitive and useful for studying the dynamics of single molecules, are not practical for SPR-like applications; rather, researchers must focus on improving the sensitivity of robust, nanoparticle-ensemble-based substrates. The report on ensembles of gold nanodiscs by Chen et al. described in section 8 represents a significant milestone along this path, as they have achieved target detection at 30 pM for prostate-specific antigen (PSA),[90] achieved through a combination of high-quality substrates and a low-noise detection scheme. Of course, the further development of such highly sensitive LSPR biosensors will ultimately be subject to the limitations of diffusion at low concentrations as described in section 5.2. In addition, the speed of throughput will be fundamentally limited by the slow binding kinetics at such low concentrations.

Another challenge that must be met before LSPR sensing can become a commercial instrument is to achieve a greater robustness of the LSPR substrates and consistency among substrates, so that analyte detection is not only specific and sensitive, but also reproducible in terms of LSPR peak wavelength and shift magnitude from substrate to substrate and experiment to experiment. Finally, for medical applications as discussed below, but also for some laboratory applications, LSPR sensors need to be able to detect analytes in complex solutions, that is, biological

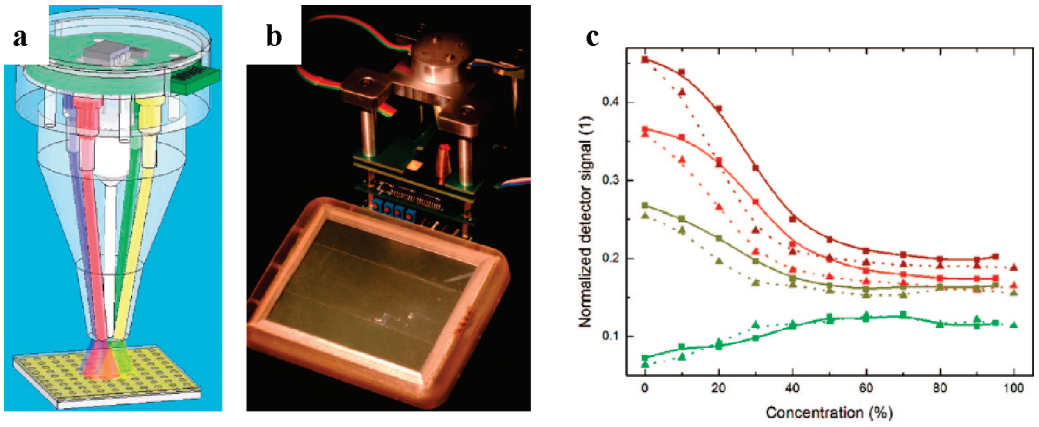

Figure 55. The portable LSPR biosensor of Neuzil and Reboud. (a) Schematic showing the four illumination LEDs. (b) Assembled sensor with 4-in. LCD screen. (c) Reflectance of LSPR chip under illumination by each of four LEDs in various water/alcohol mixtures. Reprinted with permission from ref 159. Copyright 2008 American Chemical Society.

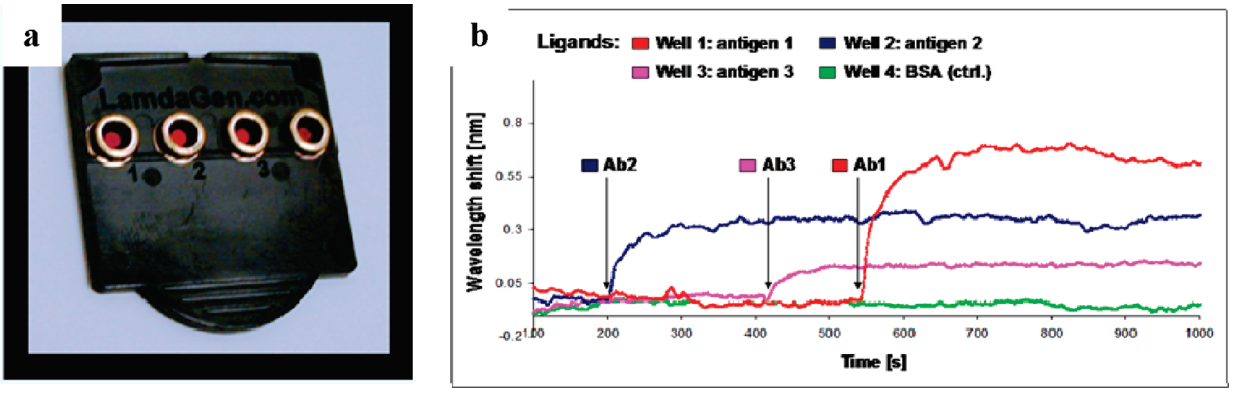

Figure 56. The LightPath S8 system measures kinetics through LSPR shifts. (a) The substrate cartridge. (b) Specific binding data measured in crude yeast extract.

samples such as blood, serum, urine, etc. This is a challenge both in terms of specificity of the sensor and a design that will allow for solutions that are not optically transparent. Glass substrates used in a reflection geometry may be best suited for this case.

A significant advantage of LSPR sensors with respect to their commercial development is their low cost. A home-built LSPR system based on white-light extinction costs less than $25,000.[33] This figure will likely be reduced with further development of the technique and instrumentation. For example, replacing the white-light spectrometer with four illumination LEDs plus a simple photodetector, as discussed in section 9.2, would greatly reduce the cost of the instrument. Further refinements, including the fiber optic and microfluidic integrations described in section 7, will extend the potential uses of benchtop LSPR sensors, and allow much smaller sample volumes to be used, also a cost-saving measure. There is an ongoing effort toward the development of commercial in vitro LSPR devices. LSPR sensor chips consisting of a nanostructured film of proprietary design are currently available.[158] LSPR substrates are reusable, unlike those for SPR, as they do not require a polymer capture layer; this represents a cost advantage in the long term use of LSPR sensors.

9.2. LSPR Sensing as a Medical Diagnostic Tool

There has been great interest in the potential of LSPR sensing as a fast, simple, low cost medical diagnostic technology. Because LSPR sensing is based on a simple optical extinction measurement, it is conceivable that robust, portable devices for point-of-care diagnostics could be developed and deployed in global outreach programs.

With an eye toward this type of application, Neuzil and Reboud have developed a hand-held device for LSPR sensing. Rather than white-light illumination and a UV−vis spectrometer, or monochromatic laser illumination, this system is based on four LEDs with well-separated emission wavelengths (525, 605, 637, and 660 nm) and a simple photodiode to measure the reflectance, greatly reducing the cost of the LSPR sensor. The signal is based on the measured reflectance intensities from the LSPR substrate for each illumination wavelength. (see Figure 55.) However, this report did not yet demonstrate detection of any biological target, but rather showed refractive index sensing for mixtures of water and ethanol or isopropoanol.[159] In this device, the sample was deposited by micropipet directly onto the LSPR chip, which was mounted ~5 mm from the light source, and could be removed, cleaned, and reused.

At least one company has also developed an LSPR-based medical prototype device. Among other demonstrations, they have shown detection of antistreptavidin, with kinetics, in various media including buffer solutions and urine (see Figure 56), with a limit of detection on the order of 1 nM.

Future challenges in the development of low-cost LSPR-based medical diagnostics may include designing substrates with greater

dx.doi.org/10.1021/cr100313v |*Chem. Rev.* 2011, 111, 3828–3857

molecular detection sensitivity, creating devices that can detect target molecules in complex fluids as described above, further miniaturizing the devices, and engineering user-friendly interfaces, in terms of both hardware and software. The ideal substrate would be reusable, easy to functionalize with the recognition element, and easy to clean and replace.

AUTHOR INFORMATION

Corresponding Author

*E-mail: hafner@rice.edu.

BIOGRAPHIES

Kathryn M. (Katie) Mayer, a native of Cleveland, OH, received her B.S. from Rice University in 2004 and her Ph.D. in 2010 as a student of Prof. Jason Hafner. Her graduate work focused on studies of membrane electrostatics by atomic force microscopy, and on biological applications of plasmon resonant nanomaterials. Since the fall of 2010, she has been a a post-doctoral researcher in the group of Prof. Kallie Willets at the University of Texas at Austin.

Jason H. Hafner is an Associate Professor of Physics and Astronomy and of Chemistry at Rice University, where his group uses the tools and materials of nanoscience to study biophysics and biotechnology. He received his B.S. from Trinity University and did his graduate research with Richard Smalley at Rice University. He returned to Rice after postdoctoral research with Charles Lieber at Harvard University.

ACKNOWLEDGMENT

We would like to thank the editors of *Chemical Reviews* for the great opportunity to carry out this review of the field. We also wish to thank all of the student and faculty members of the Laboratory for Nanophotonics at Rice University, with whom we have had many helpful discussions about LSPR sensing and plasmonics in general. We acknowledge support from the NSF funded Integrative Graduate Research and Educational Training (IGERT) program (DG0504425) in nanophotonics, and the NSF Nanoscale Science and Engineering Initiative under award number EEC-0647452.

REFERENCES

(1) Faraday, M. *Philos. Trans. R. Soc. London* **1847**, *147*, 159.
(2) Mie, G. *Ann. Phys. (Weinheim, Ger.)* **1908**, *25*, 377.
(3) Bohren, C. F.; Huffman, D. R. *Absorption and Scattering of Light by Small Particles*, 2nd ed.; Wiley-Interscience: New York, 1998.
(4) Anderson, L. J. E.; Mayer, K. M.; Fraleigh, R. D.; Yang, Y.; Lee, S.; Hafner, J. H. *J. Phys. Chem. C* **2010**, *114*, 11127.
(5) Johnson, P. B.; Christy, R. W. *Phys. Rev. B* **1972**, *6*, 4370.
(6) Horry, R.; Jardine, B. *Explore Whipple Collections*; Whipple Museum of the History of Science, University of Cambridge: UK, 2008.
(7) Thompson, D. *Gold Bull.* **2007**, *40*, 267.
(8) Jensen, T. R.; Duval, M. L.; Kelly, K. L.; Lazarides, A. A.; Schatz, G. C.; Van Duyne, R. P. *J. Phys. Chem. B* **1999**, *103*, 9846.
(9) Gans, R. *Ann. Phys. (Weinheim, Ger.)* **1912**, *37*, 881.
(10) Eustis, S.; El-Sayed, M. A. *J. Appl. Phys.* **2006**, *100*, 18243.
(11) Link, S.; El-Sayed, M. A. *J. Phys. Chem. B* **2005**, *109*, 10531.
(12) Link, S.; Mohamed, M.; El-Sayed, M. *J. Phys. Chem. B* **1999**, *103*, 3073.
(13) Nehl, C. L.; Hafner, J. H. *J. Mater. Chem.* **2008**, *18*, 2415.
(14) Mock, J. J.; Barbic, M.; Smith, D. R.; Schultz, D. A.; Schultz, S. *J. Chem. Phys.* **2002**, *116*, 6755.
(15) Zhao, J.; Pinchuk, A. O.; Mcmahon, J. M.; Li, S. Z.; Ausman, L. K.; Atkinson, A. L.; Schatz, G. C. *Acc. Chem. Res.* **2008**, *41*, 1710.
(16) Nusz, G. J.; Marinakos, S. M.; Curry, A. C.; Dahlin, A.; Hook, F.; Wax, A.; Chilkoti, A. *Anal. Chem.* **2008**, *80*, 984.
(17) Nehl, C. L.; Liao, H. W.; Hafner, J. H. *Nano Lett.* **2006**, *6*, 683.
(18) Hao, F.; Nehl, C. L.; Hafner, J. H.; Nordlander, P. *Nano Lett.* **2007**, *7*, 729.
(19) Mayer, K. M.; Lee, S.; Liao, H.; Rostro, B. C.; Fuentes, A.; Scully, P. T.; Nehl, C. L.; Hafner, J. H. *ACS Nano* **2008**, *2*, 687.
(20) Lee, S.; Mayer, K. M.; Hafner, J. H. *Anal. Chem.* **2009**, *81*, 4450.
(21) Sherry, L. J.; Chang, S.-H.; Schatz, G. C.; van Duyne, R. P. *Nano Lett.* **2005**, *5*, 2034.
(22) Sönnichsen, C.; Franzl, T.; Wilk, T.; von Plessen, G.; Feldmann, J. *Phys. Rev. Lett.* **2002**, *88*, 077402.
(23) Raschke, G.; Kowarik, S.; Franzl, T.; Sonnichsen, C.; Klar, T. A.; Feldmann, J.; Nichtl, A.; Kurzinger, K. *Nano Lett.* **2003**, *3*, 935.
(24) Becker, J.; Trugler, A.; Jakab, A.; Hohenester, U.; Sonnichsen, C. *Plasmonics* **2010**, *5*, 161.
(25) Malinsky, M. D.; Kelly, K. L.; Schatz, G. C.; Van Duyne, R. P. *J. Am. Chem. Soc.* **2001**, *123*, 1471.
(26) Haes, A. J.; Zou, S. L.; Schatz, G. C.; Van Duyne, R. P. *J. Phys. Chem. B* **2004**, *108*, 6961.
(27) Haes, A. J.; Zou, S. L.; Schatz, G. C.; Van Duyne, R. P. *J. Phys. Chem. B* **2004**, *108*, 109.
(28) Nusz, G. J.; Curry, A. C.; Marinakos, S. M.; Wax, A.; Chilkoti, A. *ACS Nano* **2009**, *3*, 795.
(29) Wild, D. *The Immunoassay Handbook*, 3rd ed.; Elsevier: Amsterdam, The Netherlands, 2005.
(30) Karlsson, R. *J. Mol. Recognit.* **2004**, *17*, 151.
(31) Fagerstam, L. G.; Frostell, A.; Karlsson, R.; Kullman, M.; Larsson, A.; Malmqvist, M.; Butt, H. *J. Mol. Recognit.* **1990**, *3*, 208.
(32) Safsten, P.; Klakamp, S.; Drake, A.; Karlsson, R.; Myszka, D. *Anal. Biochem.* **2006**, *353*, 181.
(33) Haes, A. J.; Van Duyne, R. P. *Expert Rev. Mol. Diagn.* **2004**, *4*, 527.
(34) Yonzon, C. R.; Jeoungf, E.; Zou, S. L.; Schatz, G. C.; Mrksich, M.; Van Duyne, R. P. *J. Am. Chem. Soc.* **2004**, *126*, 12669.

(35) Svedendahl, M.; Chen, S.; Dmitriev, A.; Kall, M. *Nano Lett.* **2009**, *9*, 4428.
(36) Yu, F.; Ahl, S.; Caminade, A. M.; Majoral, J. P.; Knoll, W.; Erlebacher, J. *Anal. Chem.* **2006**, *78*, 7346.
(37) Ahl, S.; Cameron, P. J.; Liu, J.; Knoll, W.; Erlebacher, J.; Yu, F. *Plasmonics* **2008**, *3*, 13.
(38) Ndieyira, J. W.; Watari, M.; Barrera, A. D.; Zhou, D.; Vogtli, M.; Batchelor, M.; Cooper, M. A.; Strunz, T.; Horton, M. A.; Abell, C.; Rayment, T.; Aeppli, G.; Mckendry, R. A. *Nat. Nanotechnol.* **2008**, *3*, 691.
(39) Chua, J. H.; Chee, R. E.; Agarwal, A.; Wong, S. M.; Zhang, G. J. *Anal. Chem.* **2009**, *81*, 6266.
(40) Jain, P. K.; Lee, K. S.; El-Sayed, I. H.; El-Sayed, M. A. *J. Phys. Chem. B* **2006**, *110*, 7238.
(41) Link, S.; El-Sayed, M. A. *J. Phys. Chem. B* **1999**, *103*, 4212.
(42) Lee, K. S.; El-Sayed, M. A. *J. Phys. Chem. B* **2006**, *110*, 19220.
(43) Chen, H. J.; Kou, X. S.; Yang, Z.; Ni, W. H.; Wang, J. F. *Langmuir* **2008**, *24*, 5233.
(44) Slaughter, L. S.; Chang, W. S.; Swanglap, P.; Tcherniak, A.; Khanal, B. P.; Zubarev, E. R.; Link, S. *J. Phys. Chem. C* **2010**, *114*, 4934.
(45) Miller, M. M.; Lazarides, A. A. *J. Phys. Chem. B* **2005**, *109*, 21556.
(46) Tam, F.; Moran, C.; Halas, N. *J. Phys. Chem. B* **2004**, *108*, 17290.
(47) Sun, Y.; Xia, Y. *Anal. Chem.* **2002**, *74*, 5297.
(48) Wang, H.; Brandl, D. W.; Le, F.; Nordlander, P.; Halas, N. J. *Nano Lett.* **2006**, *6*, 827.
(49) Underwood, S.; Mulvaney, P. *Langmuir* **1994**, *10*, 3427.
(50) Raschke, G.; Brogl, S.; Susha, A. S.; Rogach, A. L.; Klar, T. A.; Feldmann, J.; Fieres, B.; Petkov, N.; Bein, T.; Nichtl, A.; Kurzinger, K. *Nano Lett.* **2004**, *4*, 1853.
(51) Malinsky, M. D.; Kelly, K. L.; Schatz, G. C.; Van Duyne, R. P. *J. Phys. Chem. B* **2001**, *105*, 2343.
(52) Lee, J.; Hasan, W.; Odomt, T. W. *J. Phys. Chem. C* **2009**, *113*, 2205.
(53) Mock, J. J.; Smith, D. R.; Schultz, S. *Nano Lett.* **2003**, *3*, 485.
(54) Bukasov, R.; Shumaker-Parry, J. S. *Nano Lett.* **2007**, *7*, 1113.
(55) Khalavka, Y.; Becker, J.; Sonnichsen, C. *J. Am. Chem. Soc.* **2009**, *131*, 1871.
(56) Burgin, J.; Liu, M. Z.; Guyot-Sionnest, P. *J. Phys. Chem. C* **2008**, *112*, 19279.
(57) Liao, H.; Nehl, C. L.; Hafner, J. H. *Nanomedicine* **2006**, *1*, 201.
(58) Banholzer, M. J.; Harris, N.; Millstone, J. E.; Schatz, G. C.; Mirkin, C. A. *J. Phys. Chem. C* **2010**, *114*, 7521.
(59) Sherry, L. J.; Jin, R.; Mirkin, C. A.; Schatz, G. C.; Van Duyne, R. P. *Nano Lett.* **2006**, *6*, 2060.
(60) Liu, M.; Guyot-Sionnest, P. *J. Phys. Chem. B* **2005**, *109*, 22192.
(61) Kelly, K.; Coronado, E.; Zhao, L.; Schatz, G. *J. Phys. Chem. B* **2003**, *107*, 668.
(62) Liu, M. Z.; Guyot-Sionnest, P.; Lee, T. W.; Gray, S. K. *Phys. Rev. B* **2007**, *76*, 235428.
(63) McMahon, J. A.; Wang, Y. M.; Sherry, L. J.; Van Duyne, R. P.; Marks, L. D.; Gray, S. K.; Schatz, G. C. *J. Phys. Chem. C* **2009**, *113*, 2731.
(64) Jin, R. C.; Cao, Y. W.; Mirkin, C. A.; Kelly, K. L.; Schatz, G. C.; Zheng, J. G. *Science* **2001**, *294*, 1901.
(65) Mayer, K. M.; Hao, F.; Lee, S.; Nordlander, P.; Hafner, J. H. *Nanotechnology* **2010**, *21*, 255503.
(66) Unger, A.; Rietzler, U.; Berger, R.; Kreiter, M. *Nano Lett.* **2009**, *9*, 2311.
(67) Link, S.; El-Sayed, M. A. *J. Phys. Chem. B* **1999**, *103*, 8410.
(68) Lu, X. M.; Rycenga, M.; Skrabalak, S. E.; Wiley, B.; Xia, Y. N. *Annu. Rev. Phys. Chem.* **2009**, *60*, 167.
(69) Xiong, Y. J.; McLellan, J. M.; Chen, J. Y.; Yin, Y. D.; Li, Z. Y.; Xia, Y. N. *J. Am. Chem. Soc.* **2005**, *127*, 17118.
(70) Henzie, J.; Lee, M. H.; Odom, T. W. *Nat. Nanotechnol.* **2007**, *2*, 549.
(71) Liu, N.; Weiss, T.; Mesch, M.; Langguth, L.; Eigenthaler, U.; Hirscher, M.; Sonnichsen, C.; Giessen, H. *Nano Lett.* **2010**, *10*, 1103.
(72) Hao, F.; Sonnefraud, Y.; Van Dorpe, P.; Maier, S. A.; Halas, N. J.; Nordlander, P. *Nano Lett.* **2008**, *8*, 3983.
(73) Dmitriev, A.; Hagglund, C.; Chen, S.; Fredriksson, H.; Pakizeh, T.; Kall, M.; Sutherland, D. S. *Nano Lett.* **2008**, *8*, 3893.
(74) Davies, C. In *The Immunoassay Handbook*, 3rd ed.; Wild, D., Ed.; Elsevier: Amsterdam, The Netherlands, 2005.
(75) Marinakos, S. M.; Chen, S. H.; Chilkoti, A. *Anal. Chem.* **2007**, *79*, 5278.
(76) Nath, N.; Chilkoti, A. *Anal. Chem.* **2002**, *74*, 504.
(77) Haes, A. J.; Van Duyne, R. P. *J. Am. Chem. Soc.* **2002**, *124*, 10596.
(78) Nath, N.; Chilkoti, A. *Anal. Chem.* **2004**, *76*, 5370.
(79) Stewart, M. E.; Mack, N. H.; Malyarchuk, V.; Soares, J. A. N. T.; Lee, T. W.; Gray, S. K.; Nuzzo, R. G.; Rogers, J. A. *Proc. Natl. Acad. Sci. U. S.A.* **2006**, *103*, 17143.
(80) Chen, C. D.; Cheng, S. F.; Chau, L. K.; Wang, C. R. C. *Biosens. Bioelectron.* **2007**, *22*, 926.
(81) Arai, T.; Kumar, P.; Rockstuhl, C.; Awazu, K.; Tominaga, J. *J. Opt. A: Pure Appl. Opt.* **2007**, *9*, 699.
(82) Wang, Y.; Qian, W. P.; Tan, Y.; Ding, S. H. *Biosens. Bioelectron.* **2008**, *23*, 1166.
(83) Liao, W. S.; Chen, X.; Yang, T. L.; Castellana, E. T.; Chen, J. X.; Cremer, P. S. *Biointerphases* **2009**, *4*, 80.
(84) Li, X.; Jiang, L.; Zhan, Q. Q.; Qian, J.; He, S. L. *Colloids Surf., A* **2009**, *332*, 172.
(85) Kim, H. M.; Jin, S. M.; Lee, S. K.; Kim, M. G.; Shin, Y. B. *Sensors* **2009**, *9*, 2334.
(86) Hiep, H. M.; Yoshikawa, H.; Saito, M.; Tamiya, E. *ACS Nano* **2009**, *3*, 446.
(87) Hernandez, F. J.; Dondapati, S. K.; Ozalp, V. C.; Pinto, A.; O'Sullivan, C. K.; Klar, T. A.; Katakis, I. *J. Biophotonics* **2009**, *2*, 227.
(88) Dahlin, A. B.; Chen, S.; Jonsson, M. P.; Gunnarsson, L.; Kall, M.; Hook, F. *Anal. Chem.* **2009**, *81*, 6572.
(89) McPhillips, J.; Murphy, A.; Jonsson, M. P.; Hendren, W. R.; Atkinson, R.; Hook, F.; Zayats, A. V.; Pollard, R. J. *ACS Nano* **2010**, *4*, 2210.
(90) Chen, S.; Svedendahl, M.; Kall, M.; Gunnarsson, L.; Dmitriev, A. *Nanotechnology* 2009, *20*, 434015.
(91) Holmberg, A.; Blomstergren, A.; Nord, O.; Lukacs, M.; Lundeberg, J.; Uhlen, M. *Electrophoresis* **2005**, *26*, 501.
(92) Zhu, S. L.; Du, C. L.; Fu, Y. Q. *Opt. Mater.* **2009**, *31*, 1608.
(93) Yu, C. X.; Irudayaraj, J. *Anal. Chem.* **2007**, *79*, 572.
(94) Yamamichi, J.; Iida, M.; Ojima, T.; Handa, Y.; Yamada, T.; Kuroda, R.; Imamura, T.; Yano, T. *Sens. Actuators, B* **2009**, *143*, 349.
(95) Riboh, J. C.; Haes, A. J.; McFarland, A. D.; Yonzon, C. R.; Van Duyne, R. P. *J. Phys. Chem. B* **2003**, *107*, 1772.
(96) Kreuzer, M. P.; Quidant, R.; Salvador, J. P.; Marco, M. P.; Badenes, G. *Anal. Bioanal. Chem.* **2008**, *391*, 1813.
(97) Kreuzer, M. P.; Quidant, R.; Badenes, G.; Marco, M. P. *Biosens. Bioelectron.* **2006**, *21*, 1345.
(98) Kitano, H.; Anraku, Y.; Shinohara, H. *Biomacromolecules* **2006**, *7*, 1065.
(99) Kalele, S. A.; Ashtaputre, S. S.; Hebalkar, N. Y.; Gosavi, S. W.; Deobagkar, D. N.; Deobagkar, D. D.; Kulkarni, S. K. *Chem. Phys. Lett.* **2005**, *404*, 136.
(100) Hiep, H. M.; Yoshikawa, H.; Tamiya, E. *Anal. Chem.* **2010**, *82*, 1221.
(101) Haes, A. J.; Chang, L.; Klein, W. L.; Van Duyne, R. P. *J. Am. Chem. Soc.* **2005**, *127*, 2264.
(102) Guo, L. H.; Chen, G. N.; Kim, D. H. *Anal. Chem.* **2010**, *82*, 5147.
(103) Gish, D.; Nsiah, F.; McDermott, M.; Brett, M. *Anal. Chem.* **2007**, *79*, 4228.
(104) Fujiwara, K.; Watarai, H.; Itoh, H.; Nakahama, E.; Ogawa, N. *Anal. Bioanal. Chem.* **2006**, *386*, 639.
(105) Frederix, F.; Friedt, J. M.; Choi, K. H.; Laureyn, W.; Campitelli, A.; Mondelaers, D.; Maes, G.; Borghs, G. *Anal. Chem.* **2003**, *75*, 6894.
(106) Englebienne, P. *Analyst* **1998**, *123*, 1599.
(107) Endo, T.; Yamamura, S.; Nagatani, N.; Morita, Y.; Takamura, Y.; Tamiya, E. *Sci. Technol. Adv. Mater.* **2005**, *6*, 491.

(108) Chen, H. H.; Suzuki, H.; Sato, O.; Gu, Z. Z. *Appl. Phys. A: Mater. Sci. Process.* **2005**, *81*, 1127.
(109) Anker, J. N.; Hall, W. P.; Lambert, M. P.; Velasco, P. T.; Mrksich, M.; Klein, W. L.; Van Duyne, R. P. *J. Phys. Chem. C* **2009**, *113*, 5891.
(110) Karlsson, R.; Michaelsson, A.; Mattsson, L. *J. Immunol. Methods* **1991**, *145*, 229.
(111) Yoo, S. Y.; Kim, D. K.; Park, T. J.; Kim, E. K.; Tamiya, E.; Lee, S. Y. *Anal. Chem.* **2010**, *82*, 1349.
(112) Morokoshi, S.; Ohhori, K.; Mizukami, K.; Kitano, H. *Langmuir* **2004**, *20*, 8897.
(113) Haes, A. J.; Zou, S. L.; Zhao, J.; Schatz, G. C.; Van Duyne, R. P. *J. Am. Chem. Soc.* **2006**, *128*, 10905.
(114) Zhao, J.; Das, A.; Schatz, G. C.; Sligar, S. G.; Van Duyne, R. P. *J. Phys. Chem. C* **2008**, *112*, 13084.
(115) Das, A.; Zhao, J.; Schatz, G. C.; Sligar, S. G.; Van Duyne, R. P. *Anal. Chem.* **2009**, *81*, 3754.
(116) Galush, W. J.; Shelby, S. A.; Mulvihill, M. J.; Tao, A.; Yang, P. D.; Groves, J. T. *Nano Lett.* **2009**, *9*, 2077.
(117) Lin, T. J.; Huang, K. T.; Liu, C. Y. *Biosens. Bioelectron.* **2006**, *22*, 513.
(118) Li, C.; Wu, C. L.; Zheng, J. S.; Lai, J. P.; Zhang, C. L.; Zhao, Y. B. *Langmuir* **2010**, *26*, 9130.
(119) Bunka, D. H. J.; Stockley, P. G. *Nat. Rev. Microbiol.* **2006**, *4*, 588.
(120) Balamurugan, S.; Obubuafo, A.; Soper, S. A.; McCarley, R. L.; Spivak, D. A. *Langmuir* **2006**, *22*, 6446.
(121) Balamurugan, S.; Obubuafo, A.; Soper, S. A.; Spivak, D. A. *Anal. Bioanal. Chem.* **2008**, *390*, 1009.
(122) Cho, H.; Baker, B. R.; Wachsmann-Hogiu, S.; Pagba, C. V.; Laurence, T. A.; Lane, S. M.; Lee, L. P.; Tok, J. B. H. *Nano Lett.* **2008**, *8*, 4386.
(123) Mukhopadhyay, R. *Anal. Chem.* **2005**, *77*, 114a.
(124) Cheng, C. S.; Chen, Y. Q.; Lu, C. J. *Talanta* **2007**, *73*, 358.
(125) Chen, K. J.; Lu, C. J. *Talanta* **2010**, *81*, 1670.
(126) Karakouz, T.; Vaskevich, A.; Rubinstein, I. *J. Phys. Chem. B* **2008**, *112*, 14530.
(127) Nuopponen, M.; Tenhu, H. *Langmuir* **2007**, *23*, 5352.
(128) Mack, N. H.; Wackerly, J. W.; Malyarchuk, V.; Rogers, J. A.; Moore, J. S.; Nuzzo, R. G. *Nano Lett.* **2007**, *7*, 733.
(129) Jiang, H.; Markowski, J.; Sabarinathan, J. *Opt. Express* **2009**, *17*, 21802.
(130) Dubas, S. T.; Pimpan, V. *Talanta* **2008**, *76*, 29.
(131) Choi, Y.; Park, Y.; Kang, T.; Lee, L. P. *Nat. Nanotechnol.* **2009**, *4*, 742.
(132) He, X. R.; Liu, H. B.; Li, Y. L.; Wang, S.; Li, Y. J.; Wang, N.; Xiao, J. C.; Xu, X. H.; Zhu, D. B. *Adv. Mater.* **2005**, *17*, 2811.
(133) Endo, T.; Kerman, K.; Nagatani, N.; Hiepa, H. M.; Kim, D. K.; Yonezawa, Y.; Nakano, K.; Tamiya, E. *Anal. Chem.* **2006**, *78*, 6465.
(134) Yu, C. X.; Nakshatri, H.; Irudayaraj, J. *Nano Lett.* **2007**, *7*, 2300.
(135) Wang, C.; Irudayaraj, J. *Small* **2008**, *4*, 2204.
(136) Zhao, J.; Zhang, X.; Yonzon, C. R.; Haes, A. J.; Van Duyne, R. P. *Nanomedicine* **2006**, *1*, 219.
(137) Bingham, J. M.; Willets, K. A.; Shah, N. C.; Andrews, D. Q.; Van Duyne, R. P. *J. Phys. Chem. C* **2009**, *113*, 16839.
(138) Hardeberg, J. Y.; Schmitt, F.; Brettel, H. *Opt. Eng.* **2002**, *41*, 2532.
(139) Hiep, H. M.; Nakayama, T.; Saito, M.; Yamamura, S.; Takamura, Y.; Tamiya, E. *Jpn. J. Appl. Phys.* **2008**, *47*, 1337.
(140) Huang, C. J.; Bonroy, K.; Reekman, G.; Verstreken, K.; Lagae, L.; Borghs, G. *Microelectron. Eng.* **2009**, *86*, 2437.
(141) Cheng, S. F.; Chau, L. K. *Anal. Chem.* **2003**, *75*, 16.
(142) Mitsui, K.; Handa, Y.; Kajikawa, K. *Appl. Phys. Lett.* **2004**, *85*, 4231.
(143) Tang, J. L.; Cheng, S. F.; Hsu, W. T.; Chiang, T. Y.; Chau, L. K. *Sens. Actuators, B* **2006**, *119*, 105.
(144) Shao, Y. L.; Xu, S. P.; Zheng, X. L.; Wang, Y.; Xu, W. Q. *Sensors* **2010**, *10*, 3585.
(145) Anker, J. N.; Hall, W. P.; Lyandres, O.; Shah, N. C.; Zhao, J.; Van Duyne, R. P. *Nat. Mater.* **2008**, *7*, 442.
(146) Stewart, M. E.; Anderton, C. R.; Thompson, L. B.; Maria, J.; Gray, S. K.; Rogers, J. A.; Nuzzo, R. G. *Chem. Rev.* **2008**, *108*, 494.
(147) Willets, K. A.; Van Duyne, R. P. *Annu. Rev. Phys. Chem.* **2007**, *58*, 267.
(148) Hutter, E.; Fendler, J. H. *Adv. Mater.* **2004**, *16*, 1685.
(149) Haes, A. J.; Stuart, D. A.; Nie, S. M.; Van Duyne, R. P. *J. Fluoresc.* **2004**, *14*, 355.
(150) Unger, A.; Rietzler, U.; Rudiger, B.; Kreiter, M. *Nano Lett.* **2009**, *9*, 2311.
(151) Larsson, E. M.; Alegret, J.; Kall, M.; Sutherland, D. S. *Nano Lett.* **2007**, *7*, 1256.
(152) McFarland, A. D.; Van Duyne, R. P. *Nano Lett.* **2003**, *3*, 1057.
(153) Rindzevicius, T.; Alaverdyan, Y.; Dahlin, A.; Hook, F.; Sutherland, D. S.; Kall, M. *Nano Lett.* **2005**, *5*, 2335.
(154) Wang, H. Y.; Reinhard, B. M. *J. Phys. Chem. C* **2009**, *113*, 11215.
(155) Merkel, R.; Nassoy, P.; Leung, A.; Ritchie, K.; Evans, E. *Nature* **1999**, *397*, 50.
(156) Armani, A. M.; Kulkarni, R. P.; Fraser, S. E.; Flagan, R. C.; Vahala, K. J. *Science* **2007**, *317*, 783.
(157) Arnold, S.; Keng, D.; Shopova, S. I.; Holler, S.; Zurawsky, W.; Vollmer, F. *Opt. Express* **2009**, *17*, 6230.
(158) LamdaGen, 2009.
(159) Neuxil, P.; Reboud, J. *Anal. Chem.* **2008**, *80*, 6100.